

Tau lepton asymmetry by sterile neutrino emission – Moving beyond one-zone supernova models

Anna M. Suliga,^a Irene Tamborra,^a Meng-Ru Wu^{b,c}

^aNiels Bohr International Academy and DARK, Niels Bohr Institute, University of Copenhagen, Blegdamsvej 17, 2100, Copenhagen, Denmark

^bInstitute of Physics, Academia Sinica, Taipei, 11529, Taiwan

^cInstitute of Astronomy and Astrophysics, Academia Sinica, Taipei, 10617, Taiwan

E-mail: anna.suliga@nbi.ku.dk, tamborra@nbi.ku.dk, mwu@gate.sinica.edu.tw

Abstract. The mixing of active neutrinos with their sterile counterparts with keV mass is known to have a potentially major impact on the energy loss from the supernova core. By relying on a set of three static hydrodynamical backgrounds mimicking the early accretion phase and the Kelvin-Helmoltz cooling phase of a supernova, we develop the first self-consistent, radial- and time-dependent treatment of ν_s - ν_τ mixing in the dense stellar core. We follow the flavor evolution by including ordinary matter effects, collisional production of sterile neutrinos, as well as reconversions of sterile states into active ones. The dynamical feedback of the sterile neutrino production on the matter background leads to the development of a ν_τ - $\bar{\nu}_\tau$ asymmetry (Y_{ν_τ}) that grows in time until it reaches a value larger than 0.15. Our results hint towards significant implications for the supernova physics, and call for a self-consistent modeling of the sterile neutrino transport in the supernova core to constrain the mixing parameters of sterile neutrinos.

Contents

1	Introduction	1
2	Reference neutrino signal from a core-collapse supernova	2
3	Neutrino flavor conversions in the dense stellar core	4
3.1	Resonant production of sterile antineutrinos	4
3.2	Collisional production of sterile neutrinos and antineutrinos	9
4	Development of the neutrino lepton asymmetry and feedback effects	12
4.1	Radial and temporal evolution of the neutrino lepton asymmetry	12
4.2	Dynamical feedback due to the production of sterile particles	13
4.3	Impact of the production of sterile particles on the lepton asymmetry	16
4.4	Impact of the production of sterile particles on the chemical potential	18
4.5	Discussion	20
5	Outlook	21
A	Neutrino interaction rates	23
B	Neutrino conversions in the trapping regime	26

1 Introduction

Core-collapse supernovae (SNe) are amongst the most energetic and yet mysterious transients occurring in our Universe. They originate from the death of stars with mass larger than $8 M_{\odot}$. According to our current understanding, neutrinos play a pivotal role in the SN mechanism by reviving the stalled shock wave and driving the SN nucleosynthesis [1–5].

Despite the well-known importance of neutrinos in the core collapse, their behavior in the dense stellar core is not yet fully understood [1, 6]. Most importantly, current hydrodynamical SN simulations are run under the assumption that neutrino flavor conversions do not play any major role in the explosion mechanism [7–9]. Recent findings shed doubt on this ansatz, and an agreement remains to be found [10–18].

Even more fundamentally, if particles beyond the Standard Model ones exist, they may dramatically affect the SN explosion dynamics. In this context, the putative existence of extra neutrino families, such as sterile neutrinos, may have a major impact; interestingly, the existence of sterile neutrinos is compatible with current data coming from astrophysical, terrestrial, and cosmological surveys. See Refs. [19–22] for recent reviews on the topic.

Over the years, several experiments reported evidence of sterile neutrinos in various mass ranges [20, 21]. Although even eV-mass sterile neutrinos may have a non-negligible impact on the SN nucleosynthesis and dynamics [23–27], in this work we focus on sterile neutrinos with mass between 1 and 100 keV. Sterile neutrinos with mass up to $\mathcal{O}(50)$ keV are potential dark matter candidates [19, 20, 28].

If heavy sterile neutrinos exist in SNe, they could have an impact on the SN physics [27, 29–34]. At the same time, the observation of neutrinos from the SN1987A can provide bounds

on the unknown mixing parameters of the sterile particles. However, in order to derive robust constraints on keV-mass sterile neutrinos in agreement with observations, a self-consistent treatment of the sterile neutrino transport in the SN core is necessary. The latter has not been developed yet, given the major challenges induced by the modeling of the neutrino conversion physics in the extremely dense and degenerate SN core.

In this work, for the first time, we attempt to explore the effects of an extra sterile neutrino family (ν_s) with keV mass on the transport of energy and τ neutrino lepton number in the SN core self-consistently. To this purpose, we take into account the neutrino interaction rates and carefully track the flavor evolution within the SN core by including ordinary matter effects, collisional production of sterile neutrinos, as well as reconversion effects. We then explore the dynamical feedback that the production of sterile particles induces on the static SN matter background. Our aim is to explore whether a lepton asymmetry develops as a consequence of the active-sterile neutrino conversions.

The paper is organized as follows. Section 2 provides a general overview on the reference SN model adopted in this work. In Sec. 3, we model the sterile neutrino production and propagation in the stellar core without feedback effects. The generation of a $\nu_\tau - \bar{\nu}_\tau$ lepton number, and related chemical potential, due to the sterile neutrino production are explored in Sec. 4 together with the corresponding feedback on the SN physics. The impact that the previously neglected physics has on the lepton asymmetry growth is also outlined. An outlook on our findings is presented in Sec. 5. The neutrino interaction rates in the SN core, including Pauli blocking effects, are discussed in Appendix A. A derivation of the collisional production of sterile neutrinos in the dense SN core taking into account reconversions effects is presented in Appendix B.

2 Reference neutrino signal from a core-collapse supernova

In order to model the sterile neutrino production and propagation in the SN core, we rely on the inputs of a one-dimensional hydrodynamical simulation of a SN model with mass of $18.6 M_\odot$ and SFHo nuclear equation of state and gravitational mass of $1.4 M_\odot$ [35]. Given the challenges involved in the modeling of the neutrino flavor evolution under extreme conditions, we select three time snapshots from the $18.6 M_\odot$ model (corresponding to post-bounce times: $t_{\text{pb}} = 0.05, 0.5,$ and 1 s), representative of the accretion and the early Kelvin-Helmoltz cooling SN phases. In the following, we will assume the inputs from these three selected snapshots as static hydrodynamical backgrounds and explore the dynamical implications of the production of sterile particles in the SN core. Note that this is obviously an approximation since an eventual growth of the neutrino lepton asymmetry would affect the SN evolution itself. However, our work aims at gauging the impact that the sterile neutrino production has on the SN neutrino transport and dynamics. This SN model has been selected as a benchmark case; the results presented in Sec. 4 should be qualitatively similar for any SN model.

Deep in the SN core, the electron (anti-)neutrinos are highly degenerate and neutrinos are in thermal equilibrium with the SN medium. Therefore, the flavor-dependent (anti-)neutrino number densities are well described by a Fermi-Dirac distribution as a function of the neutrino energy E :

$$\frac{dn_\nu}{dE} \propto \frac{1}{2\pi^2} \frac{E^2}{e^{(E-\mu_\nu)/T} + 1}, \quad (2.1)$$

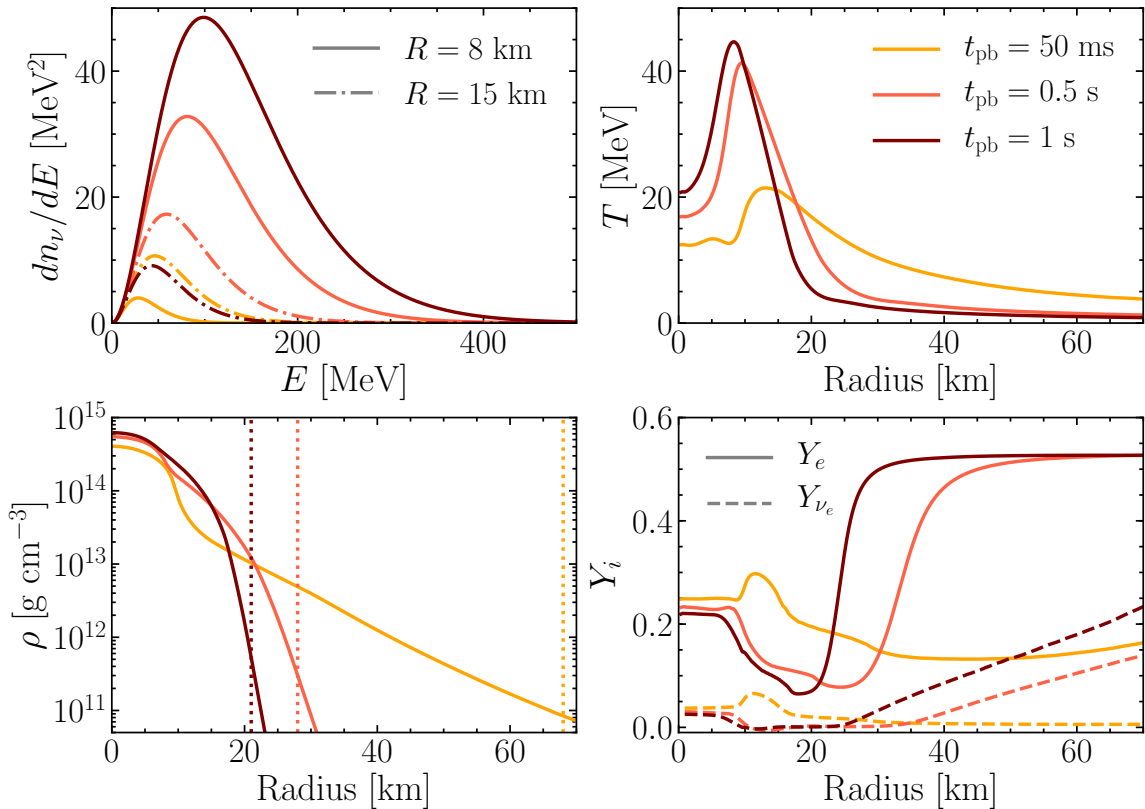


Figure 1. *Top left:* Energy distribution of ν_τ ($\bar{\nu}_\tau$) as a function of the neutrino energy for three selected post-bounce times ($t_{\text{pb}} = 0.05, 0.5$ and 1 s, in yellow, pink and brown respectively) for the $18.6 M_\odot$ SN model adopted in this work. For each time snapshot, the ν_τ distribution is plotted at 8 (continuous line) and 15 km (dash-dotted) from the stellar core, respectively. Since in the absence of active–sterile flavor conversions, $\mu_{\nu_\tau} = \mu_{\bar{\nu}_\tau} = 0$, the energy distributions of ν_τ and $\bar{\nu}_\tau$ are identical in the absence of neutrino flavor conversions. *Top right:* Radial profile of the medium temperature. *Bottom left:* Baryon density as function of the radius; the dotted vertical lines mark the ν_τ neutrinosphere radius for each t_{pb} . *Bottom right:* Electron fraction (solid lines) and electron neutrino fraction (dashed lines) as a function of the radius.

where μ_ν is the flavor-dependent neutrino chemical potential, such that $\mu_{\nu_\mu, \nu_\tau} = \mu_{\bar{\nu}_\mu, \bar{\nu}_\tau} = 0$, and T is the temperature of the SN matter. Unless otherwise specified, hereafter we will use $\hbar = c = 1$. The neutrino distribution is normalized such that $\int dE dn_\nu/dE = n_\nu$, with n_ν the local flavor-dependent neutrino number density.

The top left panel of Fig. 1 shows the energy distribution of ν_τ (identical to the one of $\bar{\nu}_\tau$) in the SN core for the three selected post-bounce times: $t_{\text{pb}} = 0.05, 0.5$, and 1 s. For each t_{pb} , the neutrino distribution is plotted at 8 and 15 km, respectively. One can see that the typical neutrino energies are $\mathcal{O}(50 - 200)$ MeV in the SN core. Moreover, for $t_{\text{pb}} = 0.05$ s, dn_ν/dE at 15 km is larger than the one at 8 km. However, this does not occur for $t_{\text{pb}} = 0.5$ and 1 s, due to the proto-neutron star contraction, see top right panel of Fig. 1. For completeness, the bottom panels of Fig. 1 show the radial profile of the baryon density on the left, and the electron fraction (Y_e) together with the electron neutrino fraction (Y_{ν_e}) on the right.

When (anti-)neutrinos decouple, their flavor-dependent energy distribution function de-

viates from a pure Fermi-Dirac distribution and it becomes pinched. It is then better represented by the following fit [36, 37]:

$$\frac{dn_\nu}{dE} \propto \left(\frac{E}{\langle E_\nu \rangle} \right)^\beta e^{-\frac{E(1+\beta)}{\langle E_\nu \rangle}}, \quad (2.2)$$

where $\langle E_\nu \rangle$ is the first energy moment, and β is the pinching parameter

$$\beta = \frac{\langle E_\nu^2 \rangle - 2\langle E_\nu \rangle^2}{\langle E_\nu \rangle^2 - \langle E_\nu^2 \rangle}, \quad (2.3)$$

depending on the second energy moment $\langle E_\nu^2 \rangle$. The normalization of Eq. 2.2 is such that $\int dE dn_\nu/dE = n_\nu$.

In the following, we use Eq. 2.1 (Eq. 2.2) to model the neutrino distribution before (after) the decoupling of neutrinos from the SN matter in the absence of flavor conversions. The decoupling radius has been defined by estimating the neutrino optical depth of τ neutrinos

$$\tau_\nu(E, r) = \int_r^\infty \sigma(E, z') n(z') dz', \quad (2.4)$$

and extracting the radius R_ν where $\tau_\nu(E, r) \simeq 1/3$. In Eq. 2.4, $\sigma(E, z')$ is the cross section in the neutrino trapping region and $n(z')$ is the number density of targets (see Appendix A).

Another useful quantity is the neutrino mean free path, defining the average distance that a neutrino with energy E can travel before interacting with other particles:

$$\lambda_\nu(E, r) \simeq \frac{1}{n(r)\sigma(E, r)}. \quad (2.5)$$

Notably, as shown in Appendix A, among the several processes involving neutrinos in the SN core, the scattering of neutrinos on nucleons ($\nu + N \rightarrow \nu + N$) is the dominant process (i.e., it dominates the interaction rate $\Gamma_\nu \simeq 1/\lambda_\nu$).

The mean free path of $\bar{\nu}_\tau$ averaged over the energy distribution is plotted as a function of the radius in Fig. 2 for $t_{\text{pb}} = 0.05, 0.5$ and 1 s. Although the mean-free path is strictly depending on the neutrino energy, one can see that the average mean free path of active (anti-)neutrinos is smaller in the SN core. On average, active neutrinos are trapped until the decoupling region (roughly marked by the neutrinosphere radius in the plot), when λ_ν becomes large enough to allow neutrinos to stream freely. The minimum of $\langle \lambda_\nu \rangle$ around 5–10 km is caused by the temperature maximum at this radius (see Fig. 1).

3 Neutrino flavor conversions in the dense stellar core

In this Section, we focus on the flavor conversions in the τ - s sector. We discuss matter effects leading to an enhanced production of sterile neutrinos, as well as collisional production of sterile neutrinos in the stellar core.

3.1 Resonant production of sterile antineutrinos

For the sake of simplicity, we work in a simplified two-flavor basis (ν_τ, ν_s). Hence, we assume there is no mixing of the sterile neutrino eigenstate with the electron and muon neutrino. We also neglect the mixing of the active neutrinos among themselves. This is, of course,

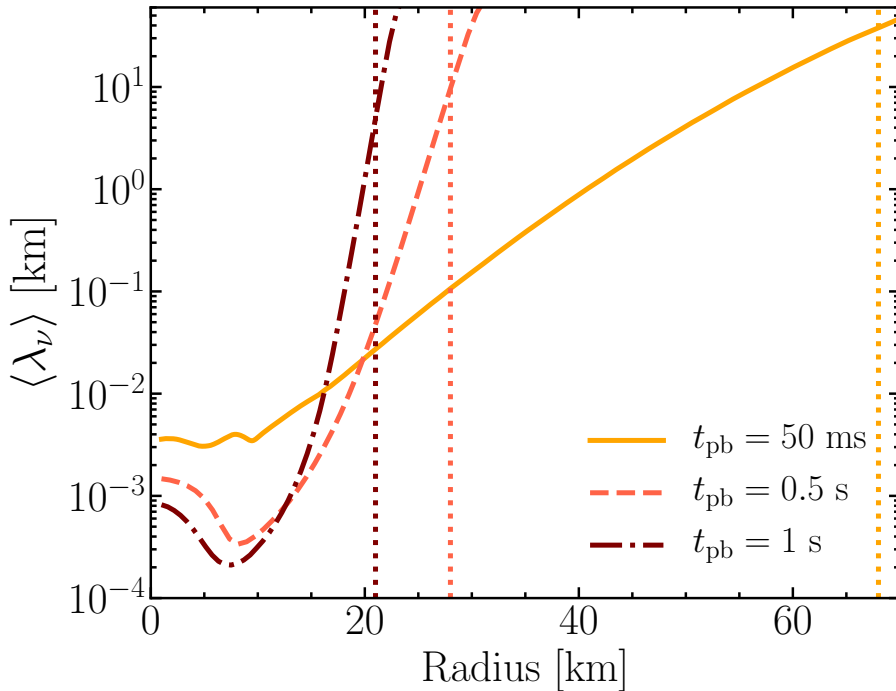


Figure 2. Energy averaged mean free path of $\bar{\nu}_\tau$ as a function of the radius for $t_{\text{pb}} = 0.05, 0.5$ and 1 s . Neutrinos are coupled to the matter in the SN core, until they reach the decoupling region roughly marked by the vertical lines indicating the ν_τ neutrinosphere radius. After decoupling, ν_τ ($\bar{\nu}_\tau$)’s stream freely.

an approximation, but it should lead to reliable results for what concerns the impact of the dynamical effects due to the sterile neutrino production on the hydrodynamical quantities. In fact, flavor conversions among the active states are expected to be suppressed in the region where active-sterile conversions occur due to the high matter density and frequent collisions with the SN medium.

The radial flavor evolution of the neutrino field is described by the Liouville equation for each energy mode E

$$\partial_r \rho_E = -i[H_E, \rho_E] + \mathcal{C}(\rho_E, \bar{\rho}_E) \text{ and } \partial_r \bar{\rho}_E = -i[\bar{H}_E, \bar{\rho}_E] + \mathcal{C}(\rho_E, \bar{\rho}_E) , \quad (3.1)$$

where the bar denotes antineutrinos and ρ is the neutrino density matrix. The density matrix for each energy mode E , ρ_E , is a 2×2 matrix in the flavor space spanned by (ν_τ, ν_s) , and similarly for antineutrinos. The initial conditions for the neutrino field are assumed to be $\rho_E = \text{diag}(n_{\nu_\tau}, 0)$ and $\bar{\rho}_E = \text{diag}(n_{\bar{\nu}_\tau}, 0)$, i.e. we work under the assumption that ν_s are only generated through mixing with ν_τ . The Hamiltonian H_E in the flavor basis takes the form

$$H_E = H_{\text{vac},E} + H_{\text{m},E} = \frac{\Delta m_s^2}{2E} \begin{bmatrix} -\cos 2\theta & \sin 2\theta \\ \sin 2\theta & \cos 2\theta \end{bmatrix} + \begin{bmatrix} V_{\text{eff}} & 0 \\ 0 & -V_{\text{eff}} \end{bmatrix} , \quad (3.2)$$

where H_{vac} is the vacuum term, function of the active-sterile mixing angle θ and the active-sterile mass difference Δm_s^2 . The effective potential V_{eff} takes into account the forward scattering potential [34]

$$V_{\text{eff}} = \sqrt{2} G_F n_B \left[-\frac{1}{2} Y_n + Y_{\nu_e} + Y_{\nu_\mu} + 2Y_{\nu_\tau} \right] , \quad (3.3)$$

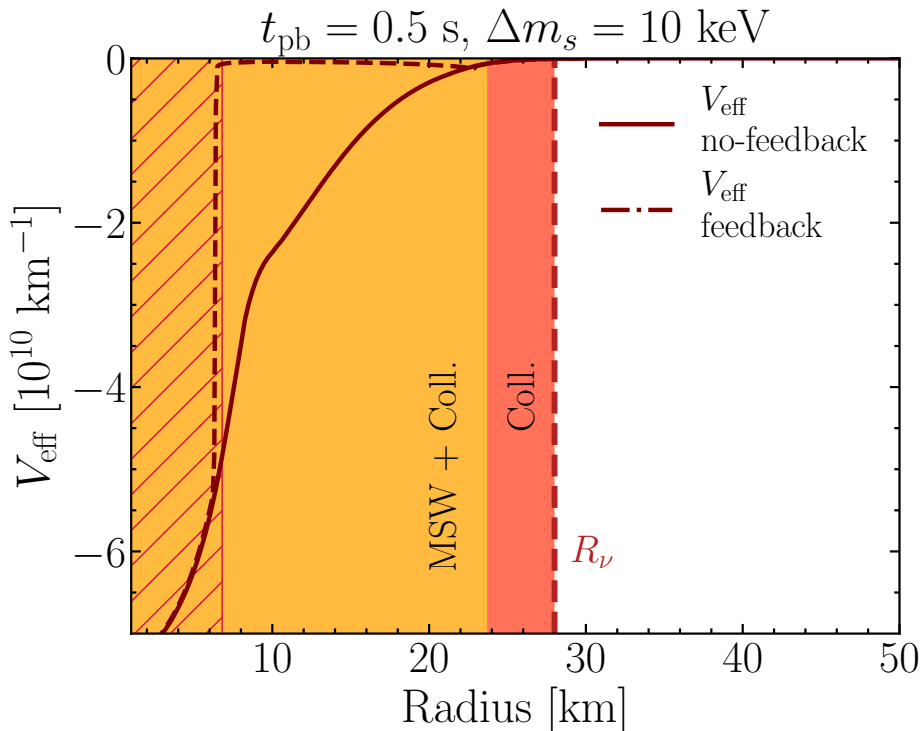


Figure 3. Neutrino-matter forward scattering potential (V_{eff}) for ν_τ - ν_s mixing as a function of the radius for $t_{\text{pb}} = 0.5$ s with (dashed, $t_{\text{pb}} + 0.03$ s, see Sec. 4 for details) feedback due to flavor conversions and in the absence of active-sterile flavor conversions (solid). The colored bands roughly indicate the region where MSW conversions are collisions are at play in yellow and the region where ν_s are produced through collisions in pink (hatched and plain bands are for the cases with and without feedback, respectively). The width of the band represents the location of the MSW resonances for different neutrino energies in the range $[0, 400]$ MeV for $\Delta m_s = 10$ keV. The collisional production becomes negligible when neutrinos start to free stream, i.e. in the correspondence of the ν_τ neutrinosphere radius (the latter is plotted in Fig. 2).

with G_F being the Fermi constant and $Y_i = (n_i - n_{\bar{i}})/n_B$, with n_i and $n_{\bar{i}}$ the number densities of the particle species i and its antiparticle \bar{i} . Since the distributions of ν_μ and $\bar{\nu}_\mu$ are identical and we neglect flavor conversions in the active sector, $Y_{\nu_\mu} = 0$ initially; however, Y_{ν_τ} may become non-zero as sterile neutrinos are generated, as it will be discussed in Sec. 4. Because of charge neutrality $Y_p = Y_e = 1 - Y_n$. Note also that the vacuum term for antineutrinos has opposite sign with respect to the one of neutrinos. The Mikheyev-Smirnov-Wolfenstein (MSW) resonance occurs at a certain distance r_{res} from the SN core, when the following condition is satisfied [38–40]:

$$\cos 2\theta = \frac{2V_{\text{eff}} E_{\text{res}}}{\Delta m_s^2}, \quad (3.4)$$

making the effective mixing angle in matter maximal.

Figure 3 shows the neutrino-matter forward scattering potential (V_{eff}) as a function of the distance from the SN core and for the representative snapshot $t_{\text{pb}} = 0.5$ s. In order to guide the eye, the orange band represents the location of the MSW resonance for neutrinos with energies up to 400 MeV and for $\Delta m_s = 10$ keV. One can immediately gauge that sterile

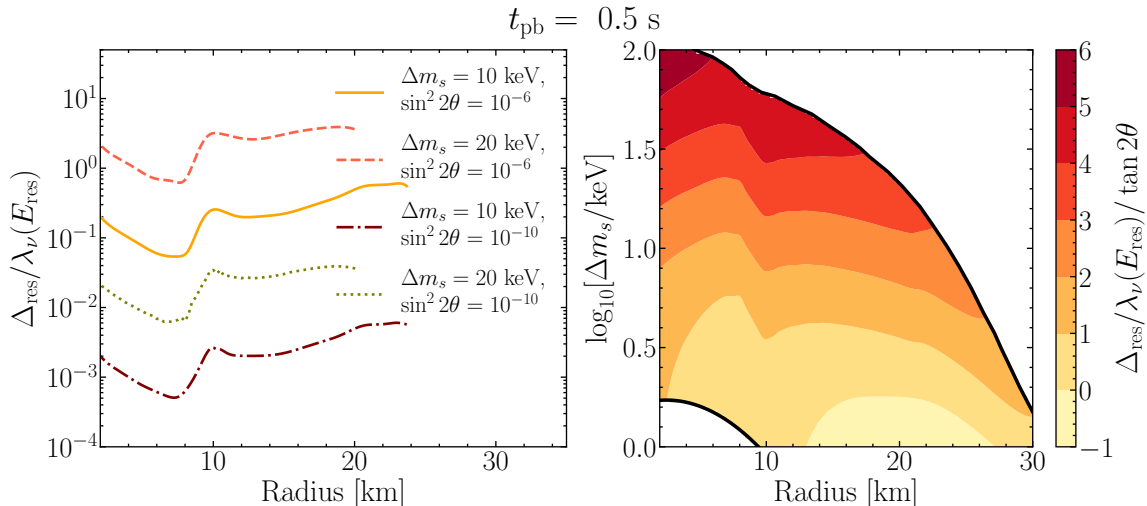


Figure 4. *Left:* Ratio of $\Delta_{\text{res}}/\lambda_{\nu}(E_{\text{res}})$ as a function of the radius for $t_{\text{pb}} = 0.5$ s for different mass-mixing parameters. When $\Delta_{\text{res}}/\lambda_{\nu}(E_{\text{res}}) > 1$, then sterile neutrinos are produced through collisions. The peak present in all curves at ~ 10 km is coming from the $\langle \lambda_{\nu} \rangle$ minimum (see Fig. 2). *Right:* Contour plot of $\Delta_{\text{res}}/(\lambda_{\nu} \tan 2\theta)$ in the plane defined by the radius and Δm_s for $t_{\text{pb}} = 0.5$ s. As the radius increases, Δ_{res} decreases because more energetic neutrinos undergo MSW resonances.

neutrinos are expected to be abundantly produced in the SN core. Moreover, given the sign of V_{eff} , the MSW resonance conditions are only obtained for $\bar{\nu}_{\tau}$ and not for ν_{τ} .

In the dense SN core, in order for the MSW resonance to occur, the neutrino mean free path (λ_{ν}) has to be sufficiently large to allow for flavor conversions, i.e. $\lambda_{\nu} \geq \Delta_{\text{res}}$, with

$$\Delta_{\text{res}} = \tan 2\theta \left| \frac{dV_{\text{eff}}/dr}{V_{\text{eff}}} \right|^{-1} \quad (3.5)$$

being the resonance width. Figure 4 shows $\Delta_{\text{res}}/\lambda_{\nu}(E_{\text{res}})$ as a function of the distance from the SN core for $t_{\text{pb}} = 0.5$ s. One can see that $\Delta_{\text{res}}/\lambda_{\nu}(E_{\text{res}}) > 1$ for certain neutrino mass-mixing parameters; if this happens, then sterile neutrinos can only be produced through collisions (see pink band in Fig. 3) as we will describe in Sec. 3.2.

When $\lambda_{\nu} \geq \Delta_{\text{res}}$, the $\nu_{\tau}-\nu_s$ conversion probability is approximated by the Landau-Zener formula [41, 42]

$$P_{\tau s}(E_{\text{res}}) = 1 - \exp\left(-\frac{\pi^2}{2}\gamma\right), \quad (3.6)$$

where $\gamma = \Delta_{\text{res}}/l_{\text{osc}}$, and with $l_{\text{osc}} = (2\pi E_{\text{res}})/(\Delta m_s^2 \sin 2\theta)$ being the oscillation length at resonance.

In order to track the radial evolution of the neutrino flavor, we use an adaptive grid made by multiple shells of width $\Delta r_{\text{step},i}$ for each neutrino energy E_i in the interval $[E_{\text{min}}, E_{\text{max}}] = [0, 1000]$ MeV. The SN shell size is determined by $\Delta r_{\text{step},i} \equiv r_i(E_i) - r_{i-1}(E_{i-1})$, where E_i and E_{i-1} are the resonance energies, and $\Delta E_i = 1$ MeV; $\Delta r_{\text{step},i} = 0.1$ km otherwise¹. For the active flavors, we assume that neutrinos are trapped for any SN shell within the neutrinosphere radius, see Fig. 2. In this static scenario (without the dynamical feedback

¹Note that we adopt an energy-dependent adaptive grid; the minimum size of Δr_{step} has been chosen to be larger than the average neutrino path between collisions and the resonant width Δ_{res} .

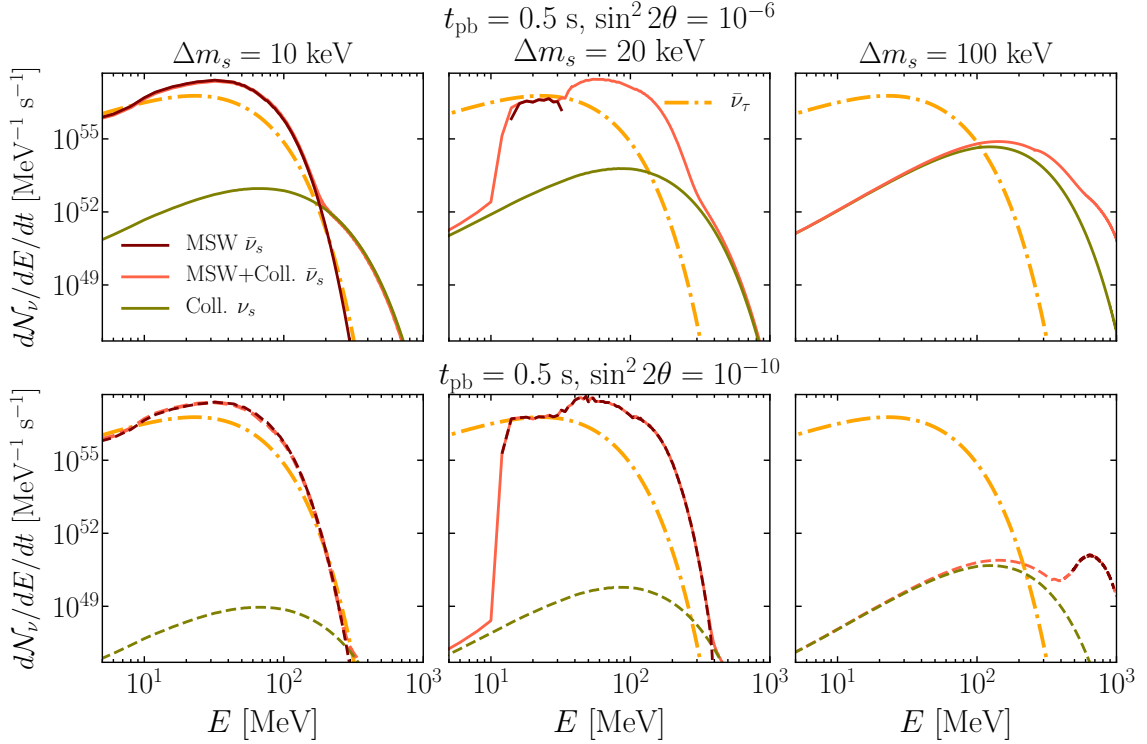


Figure 5. Sterile (anti-)neutrino energy distribution as a function of the neutrino energy after MSW conversions (in brown), MSW conversions+collisions (in pink) for $\bar{\nu}_\tau$ and only collisions for ν_τ (in green) for $t_{\text{pb}} = 0.5$ s. The mixing parameters are $\Delta m_s = 10$ keV (on the left), $\Delta m_s = 20$ keV (in the middle) and $\Delta m_s = 100$ keV (on the right), $\sin^2 2\theta = 10^{-6}$ (top panels, solid lines) and $\sin^2 2\theta = 10^{-10}$ (bottom panels, dashed lines). Additionally, the yellow dash-dotted line shows the $\bar{\nu}_\tau$ energy distribution. All distributions have been plotted at the neutrinosphere radius ($R_\nu \simeq 28$ km). Sterile particles are not produced through MSW conversions for $\sin^2 2\theta = 10^{-6}$ in the right panels (except for a tail in the high-energy part of the distribution plotted in the bottom panel) because $\Delta_{\text{res}}/\lambda_\nu > 1$. The collisional production for neutrinos and antineutrinos scales with the mixing angle due to the fact that $P_{\tau s}$ also scales with the mixing angle. Additionally in the cases where $\Delta_{\text{res}}/\lambda_\nu > 1$ the resonance width depends on the mixing angle as well.

that will be implemented in Sec. 4), we assume instantaneous replenishment of the active sector. Since in this Section we are only focusing on the radial (and not temporal) flavor evolution, sterile neutrinos are assumed to stream freely from any SN shell because of their large mean free path. In Sec. 4, where the feedback of the sterile neutrino production on the matter background will be explored, the propagation time of the sterile states across the SN shells will be taken into account together with the replenishment of active states.

The resulting energy distribution of sterile antineutrinos produced through MSW resonances at the ν_τ neutrinosphere radius is then

$$\left(\frac{d\mathcal{N}}{dE dt} \right)_{s, \text{MSW}} = \sum_{i=1}^N \Delta V_i \frac{dn_{\nu_\tau}}{dE}(r'_i) P_{\tau s}(E_{\text{res}}, r'_i) \Delta r_{\text{step}, i}^{-1}, \quad (3.7)$$

where the energy-dependent differential volume of the SN shell is $\Delta V_i = 4\pi r_i'^2 \Delta r_{\text{step}, i}$ with r_i' being the central radius on which the shell of width $\Delta r_{\text{step}, i}$ is centered. The sum across the SN shells runs from the center of the SN core until the neutrinosphere radius R_ν (i.e.,

$[r_1, r_N] = [1 \text{ km}, R_\nu]$). Note that, since sterile neutrinos do not interact and stream freely as soon as they are produced, this is the actual number of sterile particles per unit energy and time at R_ν .

Figure 5 shows the energy distribution for τ and sterile neutrinos and antineutrinos at $t_{\text{pb}} = 0.5 \text{ s}$ after MSW conversions (in brown) for $\Delta m_s = 10 \text{ keV}$ (on the left), $\Delta m_s = 20 \text{ keV}$ (in the middle), and $\Delta m_s = 100 \text{ keV}$ (on the right), $\sin^2 2\theta = 10^{-6}$ (top panels, solid lines) and $\sin^2 2\theta = 10^{-10}$ (bottom panels, dashed lines). For comparison, the yellow dash-dotted line shows the $\bar{\nu}_\tau$ energy distribution in the absence of flavor conversions. All distributions have been plotted at the neutrinosphere radius ($R_\nu \simeq 28 \text{ km}$, see Fig. 2). Given the sign of the effective matter potential, only $\bar{\nu}_s$'s are produced through MSW conversions. The $\bar{\nu}_s$ energy distributions for $\Delta m_s = 20 \text{ keV}$ are affected by MSW conversions only above 12 MeV; in fact, lower energy modes do not undergo MSW resonances. Sterile antineutrinos are not produced through MSW conversions for $\Delta m_s = 100 \text{ keV}$, except for a small fraction around 1000 MeV because $\Delta_{res}/\lambda_\nu > 1$, i.e. $\bar{\nu}_\tau$'s interact with the matter background before to convert into sterile states.

The cumulative luminosity converted in sterile antineutrinos via MSW transitions at the distance r from the SN core is

$$L_{s,\text{MSW}} = \sum_{j=1}^M \sum_{k=1}^L \Delta E_k \Delta V_j E_{\text{res}}(r'_j) \frac{dn_{\nu_\tau}}{dE_k}(r'_j) P_{\tau s}(E_{\text{res}}, r'_j) \Delta r_{\text{step},j}^{-1}, \quad (3.8)$$

where $[r'_{j=1}, r'_{j=M}] = [1 \text{ km}, r]$ and $[E_{k=1}, E_{k=L}] = [E_{\text{min}}, E_{\text{max}}]$, $\Delta E_k = \Delta E = 1 \text{ MeV}$. Figure 6 shows the cumulative luminosity emitted in sterile antineutrinos due to MSW conversions (in brown) for the same mass and mixing parameters shown in Fig. 5. As expected from Fig. 3, MSW flavor conversions mainly occur in the SN core up to 10–20 km according to the mixing. Notably, in all cases described here $\bar{\nu}_\tau$'s undergo only one MSW resonance. In fact, in the absence of collisions, the probability that $\bar{\nu}_s$'s reconvert in $\bar{\nu}_\tau$'s is zero. As we will see in Sec. 3.2, reconversion effects are not negligible in the presence of collisions. In the $\Delta m_s = 10 \text{ keV}$ panel, the cumulative luminosity due to MSW conversions reaches a stationary value at $\simeq 20 \text{ km}$, i.e. when MSW conversions become irrelevant. A similar behavior occurs for $\Delta m_s = 20$ and 100 keV.

3.2 Collisional production of sterile neutrinos and antineutrinos

Given the high matter density in the SN core, active (anti-)neutrinos are trapped because of collisions, see e.g. [43]. In the trapping regime, the neutrino propagation eigenstate is a mixture of active and sterile states; due to scattering on nucleons, the propagation eigenstate collapses to a pure flavor eigenstate. Sterile states can therefore be produced through collisions. After that, the sterile states may be reconverted back to τ (anti-)neutrinos through MSW conversions.

The effective conversion probability including the effect of collisions is

$$\langle P_{\tau s}(E, r) \rangle \approx \frac{1}{4} \frac{\sin^2 2\theta}{(\cos 2\theta - 2V_{\text{eff}}E/\Delta m_s^2)^2 + \sin^2 2\theta^2 + D^2}, \quad (3.9)$$

where D is the quantum damping term,

$$D = \frac{E\Gamma_\nu(E)}{\Delta m_s^2}; \quad (3.10)$$

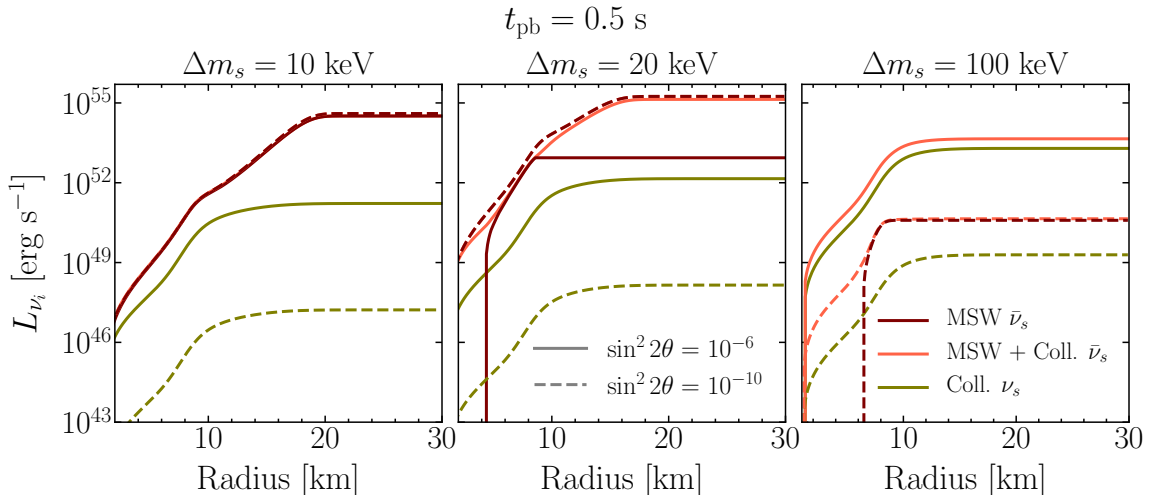


Figure 6. Cumulative luminosity of sterile neutrinos and antineutrinos as a function of the SN radius after MSW conversions (in brown), MSW conversions+collisions (in pink) for antineutrinos and only collisions for neutrinos (in green) for $t_{\text{pb}} = 0.5$ s and mixing parameters $\Delta m_s = 10$ keV (on the left), $\Delta m_s = 20$ keV (in the middle), $\Delta m_s = 100$ keV (on the right), and for $\sin^2 2\theta = 10^{-6}$ (solid lines) and $\sin^2 2\theta = 10^{-10}$ (dashed lines). Most of the production of sterile particles occurs within 10–20 km for all the mass and mixings considered here. The collisional production of sterile particles has a non-negligible impact as Δm_s increases. See Fig. 5 for comparison.

the collision rate for ν_τ undergoing neutral current (NC) scatterings is defined as detailed in Appendix A:

$$\Gamma_\nu(E) = n_B [F_p(E)Y_e\sigma_{\nu p}(E) + F_n(E)(1 - Y_e)\sigma_{\nu n}(E)] , \quad (3.11)$$

where $F_{p,n}(E)$ represents the Pauli blocking factor estimated as in Appendix A. Note that, except for the correction due to collisions, Eq. 3.9 is defined through the effective conversion probability of neutrinos in matter. The factor 1/4 in Eq. 3.9 takes into account a factor 1/2 to average the overall probability due to flavor oscillations, and another factor 1/2 coming from taking into account the detailed balance equilibrium conditions in the SN core [43]; note that since we include the detailed balance correction factor in $\langle P_{\tau s}(E, r) \rangle$ instead than in Eq. 3.11, Eq. 3.9 is slightly different than what has been reported in the literature, see e.g. [44]. Equation 3.9 is such that when the damping term is large, no flavor conversion occurs and the system will be frozen in its initial state.

Figure 2 indicates that two scenarios are possible for active neutrinos: Either they stream freely out of the SN shell or they are trapped and undergo collisions with the dense SN matter. In the latter case, if $\lambda_\nu \ll \Delta r_{\text{step}}$, neutrinos undergo multiple collisions within each SN shell of width Δr_{step} . The same situation can in fact happen for sterile neutrinos.

Once produced, according to their mean free path, sterile neutrinos can either free stream or collide and reconvert back to active states, especially in the SN shells where favorable conditions for MSW resonances exist; unlike sterile neutrinos produced through MSW effects in the absence of collisions (see previous Section). To model this effect, we divide each SN shell of width Δr_{step} into sub-shells of width λ_ν . The number of sub-shells within Δr_{step} is

$$n = \left\lceil \frac{\Delta r_{\text{step}}}{\lambda_\nu} \right\rceil . \quad (3.12)$$

This allows to take into account the reconversion of (anti-) ν_s to (anti-) ν_τ within the sub-shells. The effective conversion probability has been derived in Appendix B and it is

$$P_{\tau s}(E, n) = \frac{1}{n} \sum_{k=1}^n \langle P_{\tau s} \rangle (1 - \sin^2 2\tilde{\theta} \langle P_{\tau s} \rangle)^{k-1}, \quad (3.13)$$

with $\tilde{\theta}$ being the effective mixing angle in matter, under the assumption that the matter potential is constant within each SN shell (see Appendix B for details). Equation 3.13 indicates that the effective conversion probability is smaller as n increases; moreover, for $n = 1$, one recovers the case $P_{\tau s}(E, 1) = \langle P_{\tau s} \rangle$ for $\lambda_\nu \simeq \Delta r_{\text{step}}$. Equation 3.13 includes the reconversion of sterile into active states due to multiple collisions through $\langle P_{\tau s} \rangle$.

The corresponding energy distribution of sterile (anti-)neutrinos produced through collisions until the ν_τ neutrinosphere radius is

$$\left(\frac{d\mathcal{N}}{dE dt} \right)_{s, \text{coll}} = \sum_{i=1}^N \Delta V_i \frac{dn_{\nu_\tau}}{dE}(r'_i) n P_{\tau s}(E, n, r'_i) \Delta r_{\text{step}, i}^{-1}. \quad (3.14)$$

Figure 5 shows the sterile neutrino energy distributions for the cases where MSW resonant conversions as well as collisions are taken into account for antineutrinos (in pink) and for neutrinos (collisions only, in green) for $t_{\text{pb}} = 0.5$ s. While the MSW conversions only affect the $\bar{\nu}_s$ energy distribution as discussed in Sec. 3.1, the collisional production occurs for neutrinos and antineutrinos. As we will discuss in Sec. 4, this implies that the development of a neutrino lepton asymmetry is only possible in the presence of MSW resonances or MSW enhanced collisions. The pink line in Fig. 5 for 10 keV and $\sin^2 2\theta = 10^{-10}$ (left, bottom panel) lies very close to the green one for energies > 250 MeV, i.e. the energy distribution is dominated by the collisional contribution at those high energies. In fact, antineutrinos produced through collisions before the MSW layer reconvert back to $\bar{\nu}_\tau$ for fully adiabatic MSW resonances; however, this may not be the case according to the adiabaticity of MSW conversions and frequency of collisions (see $\Delta_{\text{res}}/\lambda_\nu(E_{\text{res}})$ in Fig. 4). As the neutrino energy increases, the MSW conversions stop being fully adiabatic for $\sin^2 2\theta = 10^{-10}$; hence, not all $\bar{\nu}_s$'s produced before the MSW layer reconvert to active ones. In the fully adiabatic case ($\sin^2 2\theta = 10^{-6}$, top left panel), the pink line lies slightly below the green one because of reconversions. The collisional production dominates the high energy tail of the energy distribution also for $\Delta m_s = 20$ keV. On the other hand, at all energies, antineutrinos produced through collisions are more abundant than the ones produced through MSW conversions for $\Delta m_s = 100$ keV.

Similarly to Eq. 3.8, the cumulative luminosity emitted in sterile (anti-)neutrinos through collisional production is

$$L_{s, \text{coll}} = \sum_{j=1}^M \sum_{k=1}^L \Delta V_j \Delta E_k \frac{dn_{\nu_\tau}}{dE_k}(r'_j) E_k \Delta r_{\text{step}, j}^{-1} n P_{\tau s}(E_k, n, r'_j), \quad (3.15)$$

where the numerical inputs adopted for ΔE , Δr_{step} , and the integrations over radius and energy are the same as defined in Sec. 3. Due to the reconversion effects, the overall production of sterile particles may be suppressed according to the mixing parameters.

Figure 6 shows the cumulative luminosity emitted in sterile particles, due to MSW conversions+collisions for antineutrinos (in pink) and only due to collisions for neutrinos (in green), as a function of the radius for the same mass and mixing parameters shown in Fig. 5.

In the left panel, the MSW only case (brown curve) leads to $L_{\bar{\nu}_s}$ that is identical to the case of MSW conversions+collisions (pink curve); in fact, reconversions are only relevant for very high energies and have a negligible impact on the overall luminosity. As also visible from Fig. 3, collisions are important in the SN core where neutrinos are trapped and negligibly affect the sterile neutrino luminosity at radii larger than 10 km for all mass and mixing parameters shown here. In the $\Delta m_s = 10$ keV panel, the pink line shows a bump at $\simeq 10$ km, i.e. in correspondence of the radius where collisions stop being dominant and the medium temperature reaches its maximum. The collisional production of sterile particles has a non-negligible impact as Δm_s increases, see e.g. the $\Delta m_s = 100$ keV panel on the right where the particle production is dominated by collisions. In the $\Delta m_s = 20$ keV panel for $\sin^2 2\theta = 10^{-6}$, one can see that the pink line is considerably above the green and the brown ones for $\sin^2 2\theta = 10^{-6}$ because the resonant layer is collisionally enhanced (i.e., $\Delta r_{\text{res}}/\lambda_\nu > 1$, see Fig. 4). In the right panel, one can see that the collisional production is the main mechanism producing sterile particles for $\sin^2 2\theta = 10^{-6}$.

4 Development of the neutrino lepton asymmetry and feedback effects

In this Section, we explore the dynamical feedback that the production of sterile particles induces on the growth of Y_{ν_τ} and, in turn, on the flavor conversion physics. First, we detail the treatment of the dynamical feedback on the growth of Y_{ν_τ} in Sec. 4.1. Then, in Secs. 4.2 and 4.3, we explore the effect of the net Y_{ν_τ} generation on the effective potential felt by neutrinos and the associated sterile neutrino production. In Sec. 4.4, we further discuss results derived when the feedback effects coming from the net lepton number Y_{ν_τ} , as well as the ν_τ chemical potential (μ_{ν_τ}) are taken into account. For the sake of simplicity, we rely on a static hydrodynamical background for the three selected snapshots of the $18.6 M_\odot$ model, and investigate the radial and temporal evolution of the neutrino lepton asymmetry and its corresponding impact on the matter potential V_{eff} .

4.1 Radial and temporal evolution of the neutrino lepton asymmetry

Sterile neutrinos and antineutrinos are produced at the expense of τ neutrinos and antineutrinos. As discussed in Sec. 3, MSW (collisionally enhanced) transitions affect neutrinos and antineutrinos differently, leading to the development of $Y_{\nu_\tau} \neq 0$. One can see from Eq. 3.3, and by comparing the continue and the dashed lines of Fig. 3, that any variation of Y_{ν_τ} can substantially affect V_{eff} . In turn, the modified V_{eff} has an impact on the flavor conversion evolution.

To investigate the dynamical feedback due to the growth of Y_{ν_τ} on V_{eff} , we rely on the static hydrodynamical inputs of the three time snapshots of the $18.6 M_\odot$ SN model: $t_{\text{pb}} = 0.05, 0.5$ and 1 s; for each time snapshot, we track the flavor evolution in r as described in Sec. 3 simultaneously with the radial evolution of Y_{ν_τ} . The V_{eff} obtained by $Y_{\nu_\tau} \neq 0$ is then adopted as input for the next temporal step. This allows to explore how Y_{ν_τ} evolves in time t . Hence, although we rely on static hydrodynamical inputs for the sake of simplicity, we explore the dynamical feedback of the production of sterile particles self-consistently, by following the time and radial evolution of the relevant quantities.

For fixed t_{pb} and r , we compute the evolution of Y_{ν_τ} after a time interval Δt by tracking

the flavor evolution as described in Sec. 3 and by solving the following equation simultaneously

$$Y_{\nu_\tau}(r, t_{\text{pb}} + \Delta t) = \frac{1}{n_B(r)} \sum_{l=1}^P \sum_{k=1}^L \left[\bar{P}_{\tau s}(E_k, t'_l) \frac{dn_{\bar{\nu}_\tau}}{dE_k}(t'_l, \Delta r_{\text{step}}) - P_{\tau s}(E_k, t'_l) \frac{dn_{\nu_\tau}}{dE_k}(t'_l, \Delta r_{\text{step}}) \right] \times \Delta E_k \Delta r_{\text{step}}^{-1} \Delta t'_l, \quad (4.1)$$

where $[t_{l=1}, t_{l=P}] = [t_{\text{pb}}, t_{\text{pb}} + \Delta t]$, $[E_{k=1}, E_{k=L}] = [E_{\text{min}}, E_{\text{max}}]$, $\bar{P}_{\tau s}$ is the antineutrino conversion probability (Eqs. 3.6, 3.13) and $P_{\tau s}$ is the neutrino conversion probability (Eq. 3.13); $dn_{\nu_\tau}/dE(t', \Delta r_{\text{step}})$ is the local density of particles in Δr_{step} , per unit energy. The radial step assumed in this calculation including the dynamical feedback is $\Delta r_{\text{step}} \simeq 0.1$ km; if $\Delta r_{\text{res}} \geq 0.1$ km for certain energies, then we assume $\Delta r_{\text{step}} = \Delta r_{\text{res}}$. The energy step is $\Delta E = E_{\text{res}}(r_i + \Delta r_{\text{step}}) - E_{\text{res}}(r_i)$ for the MSW conversions and the MSW enhanced collisional production; instead for collisions outside the resonance, $\Delta E = 2$ MeV.

The time step adopted in the numerical runs is $\Delta t' = 10^{-7}$ s. Sterile neutrinos produced in the trapping regime ($r < R_\nu$) take $t'_* = R_\nu/c \simeq 10^{-4}$ s $\gg \Delta t'$ to escape from the neutrinosphere. Hence, for the sake of simplicity, we let all sterile particles to stream freely from the neutrinosphere every t'_* (while keep them trapped in the production SN shell for smaller times), including the reconversion effects. In order to take into account the replenishment of τ (anti-)neutrinos through Bremsstrahlung (see Appendix A for details), we limit the sterile neutrino production rate by the Bremsstrahlung one if the production rate of sterile particles is larger than $\Gamma_{NN \rightarrow NN\nu_\tau\bar{\nu}_\tau}$.

4.2 Dynamical feedback due to the production of sterile particles

In the following, we investigate the role of the dynamical feedback on Y_{ν_τ} and on the sterile production, by focusing on the benchmark time snapshot $t_{\text{pb}} = 0.5$ s for $(\Delta m_s, \sin^2 2\theta) = (10 \text{ keV}, 10^{-10})$. We will generalize our findings to the three considered t_{pb} and other $(\Delta m_s, \sin^2 2\theta)$ in Sec. 4.3. Note that, in this subsection and in Sec. 4.3, we take into account the feedback effects by updating the effective potential V_{eff} via Eq. (3.3), while keeping the ν_τ and $\bar{\nu}_\tau$ energy distributions unaffected in Eq. (4.1). However, $Y_{\nu_\tau} \neq 0$ is also responsible for the growth of $\mu_{\nu_\tau} \neq 0$, which in turn would dynamically modify the (anti-)neutrino energy distributions; results obtained by including the dynamical feedback of Y_{ν_τ} and μ_{ν_τ} are discussed in Sec. 4.4.

The left panel of Fig. 7 shows a comparison between the Y_{ν_τ} obtained without any dynamical feedback effect due to the sterile neutrino production (dashed line), as described in Sec. 3, and the one obtained by tracking the radial and temporal evolution of Y_{ν_τ} as from Eq. 4.1 (continuous line). Note that Y_{ν_τ} has been divided by 100 in the former case. The continuous lines with different hues mark the temporal evolution (from lighter to darker as time increases) within $\Delta t = 0.03$ s. It shows that Y_{ν_τ} quickly reaches stationary values after ~ 0.01 s in the region between 10–20 km, and a plateau of $Y_{\nu_\tau} \simeq 0.21$ develops. The plateau continues to extend to smaller radii as time progresses. We consider $\Delta t = 0.03$ s, since after such a time interval, Y_{ν_τ} has reached its stationary radial profile. As t' increases, the Y_{ν_τ} plateau extends towards the inner core of the SN. In fact, as t' increases, high-energy modes undergo MSW resonances (as we will discuss, this is also visible in the right panel of Fig. 8). The sharp growth of Y_{ν_τ} at small radii is due to the fact that Y_{ν_τ} evolves towards its stationary profile because of MSW (collisionally enhanced) conversions, but only energy modes higher than a certain energy undergo resonances. Moreover, the production of sterile

$$t_{\text{pb}} = 0.5 + \Delta t \text{ s}, \quad \Delta m_s = 10 \text{ keV}, \quad \sin^2 2\theta = 10^{-10}$$

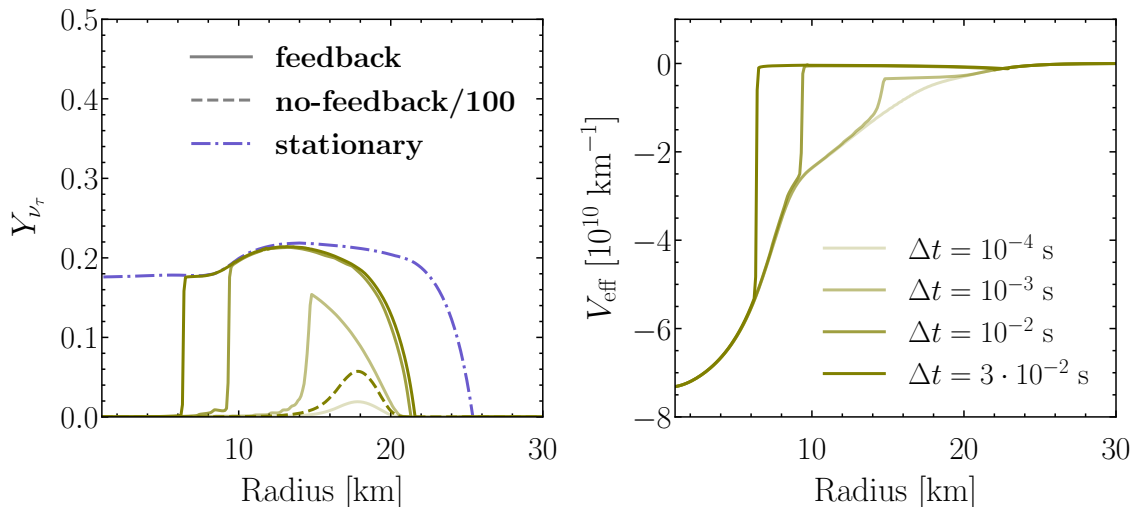


Figure 7. *Left:* Radial profile of Y_{ν_τ} for $t_{\text{pb}} = 0.5 \text{ s}$, $(\Delta m_s, \sin^2 2\theta) = (10 \text{ keV}, 10^{-10})$; the dashed line is for the case without feedback ($\Delta t = 0$) and continuous line for the case with feedback due to the production of sterile particles ($\Delta t = 0.03 \text{ s}$). The continuous lines with different hues mark the temporal evolution (from lighter to darker as time increases). The dash-dotted purple curve shows the $Y_{\nu_\tau}^{\text{stat}}$ for $E_{\text{max}} = 1000 \text{ MeV}$ estimated analytically (see text for details). *Right:* Corresponding radial profile of V_{eff} for the case with feedback. The dynamical feedback due flavor conversions in sterile states considerably affects Y_{ν_τ} and V_{eff} .

particles becomes slower because of Pauli blocking effects (see middle panel of Fig. 17). Importantly, Y_{ν_τ} is largely overestimated when the dynamical feedback effects are not taken into account.

At the same time, V_{eff} (see Eq. 3.3) follows the Y_{ν_τ} evolution, hence the radial evolution of V_{eff} is strongly affected, as shown in the right panel of Fig. 7. The stationary value of Y_{ν_τ} is reached when $V_{\text{eff}} \rightarrow 0$ and no more conversions into sterile states occur, i.e. Y_{ν_τ} does not change further. To verify this, we have analytically computed the stationary Y_{ν_τ} value ($Y_{\nu_\tau}^{\text{stat}}$) at each radius by equating V_{eff} (Eq. 3.3) to $(\Delta m_s^2 \cos 2\theta)/2E_{\text{max}}$. The dash-dotted purple curve in Fig. 7 shows the $Y_{\nu_\tau}^{\text{stat}}$ as a function of the radius obtained for $E_{\text{max}} = 1000 \text{ MeV}$. It clearly illustrates that, in the SN core, the sterile neutrino productions leads to the evolution of Y_{ν_τ} towards a stationary value. We note that for the inner part ($r \lesssim 6 \text{ km}$) and the outer part ($r \gtrsim 20 \text{ km}$), it takes longer than $\sim 0.03 \text{ s}$ for Y_{ν_τ} to reach $Y_{\nu_\tau}^{\text{stat}}$, due to the slower production rate of sterile neutrinos. As one can see from this example, the dynamical feedback of flavor conversions considerably modifies Y_{ν_τ} and V_{eff} . As shown in Fig. 3, because of the evolution of V_{eff} in time, neutrinos interact with a different effective matter background, and the radial regions where MSW resonances occur evolve accordingly.

Due to the Y_{ν_τ} temporal evolution, the sterile (anti-)neutrino production is in turn affected. Figure 8 shows contour plots of the number density of $\bar{\nu}_s$'s (on the top) and ν_s 's (on the bottom) in the plane defined by the radius and the neutrino energy for $\Delta t = 0$ on the left and $\Delta t = 0.03 \text{ s}$ on the right. The left panels represent the sterile number densities obtained by neglecting the dynamical feedback effects due to the production of $Y_{\nu_\tau} \neq 0$ on V_{eff} , as described in Sec. 3. The impact of the dynamical feedback on the sterile number density is

$$t_{\text{pb}} = 0.5 + \Delta t \text{ s}, \quad \Delta m_s = 10 \text{ keV}, \quad \sin^2 2\theta = 10^{-10}$$

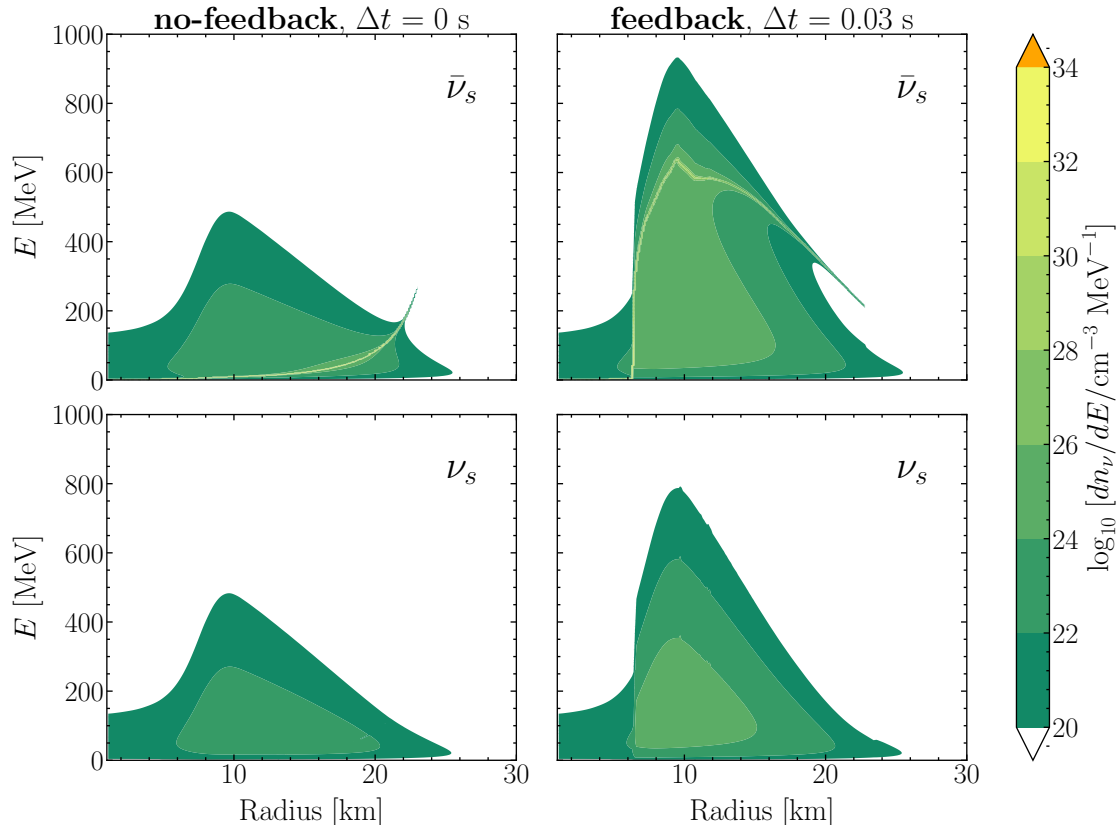


Figure 8. Contour plots of the number density of $\bar{\nu}_s$'s (top panels) and ν_s 's (bottom panels) per unit energy in the plane spanned by the distance from the SN core and the neutrino energy for $(\Delta m_s, \sin^2 2\theta) = (10 \text{ keV}, 10^{-10})$, $t_{\text{pb}} = 0.5 \text{ s}$. *Left:* Without any dynamical feedback effect due to the production of sterile particles ($\Delta t = 0$), see Sec. 3. *Right:* With dynamical feedback effect due to the production of sterile particles ($\Delta t = 0.03 \text{ s}$). The dynamical modification of V_{eff} due to the production of sterile particles drastically affects the local density of sterile (anti-)neutrinos. The light green line in the plots on the top panels marks the location of the MSW resonances.

shown in the panel on the right. One can see that a light green line visible at the center of the contour plot for $\bar{\nu}_s$'s; this is due to the resonant production of sterile antiparticles. Moreover, the dynamical modification of V_{eff} due to the production of sterile particles drastically affects the local density of sterile antineutrinos since the temporal evolution of V_{eff} triggers the MSW (collisionally enhanced) production of $\bar{\nu}_s$'s with higher energies (see also Fig. 7).

As discussed for Figs. 3 and 7, the temporal evolution of V_{eff} affects the radial range where MSW resonances occur. This is also visible in Fig. 9 where the cumulative luminosities of ν_s and $\bar{\nu}_s$ have been plotted for the feedback case with $\Delta t = 0.03 \text{ s}$ and for the case without feedback (see also left panel of Fig. 6). The overall production of ν_s 's is lower than the one of $\bar{\nu}_s$'s similarly to the case without feedback because MSW effects only take place for antineutrinos. However, given the change in shape of V_{eff} (see right panel of Fig. 7) because of the dynamical feedback, flavor conversions occur deeper inside in the SN core as time progresses.

Figure 10 shows the temporal evolution of the production rate of sterile (anti-)neutrinos,

$$t_{\text{pb}} = 0.5 + \Delta t \text{ s}, \quad \Delta m_s = 10 \text{ keV}, \quad \sin^2 2\theta = 10^{-10}$$

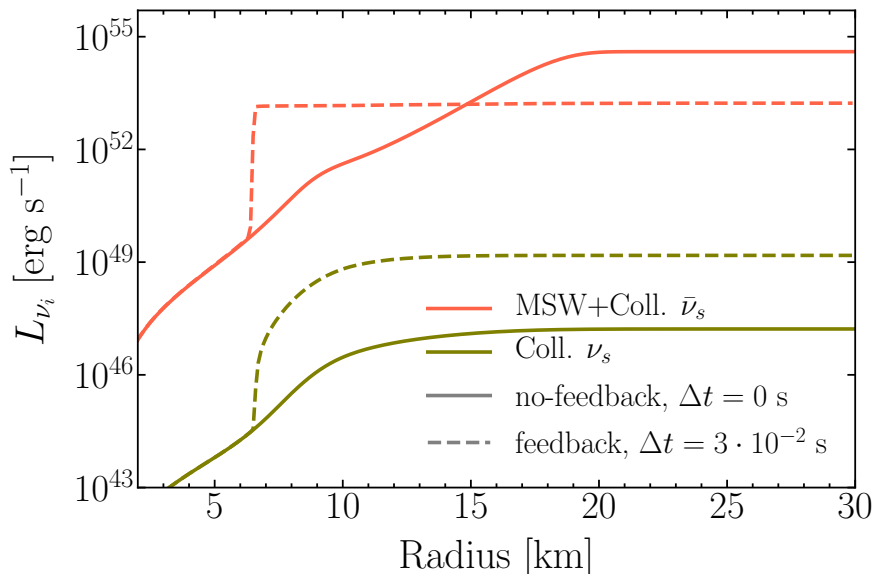


Figure 9. Cumulative luminosity of sterile neutrinos and antineutrinos as a function of the SN radius for $t_{\text{pb}} = 0.5 \text{ s}$ and mixing parameters $\Delta m_s = 10 \text{ keV}$ and $\sin^2 2\theta = 10^{-10}$ with dynamical feedback effect due to the production of sterile particles (dashed, $\Delta t = 0.03 \text{ s}$) and without feedback (continuous, $\Delta t = 0$). The radial region where sterile particles are produced is affected by the feedback effects. Most of the production of sterile particles occurs within 10–20 km for all the mass and mixings considered here. The corresponding cumulative luminosity for the case without feedback is also shown in the left panel of Fig. 6.

dN_{ν_s}/dt and $dN_{\bar{\nu}_s}/dt$, at $R_\nu = 28 \text{ km}$. One can see that, the self-consistent implementation of the dynamical feedback effects leads to a quenching of $d(N_{\nu_s} + N_{\bar{\nu}_s})/dt$ after a certain time, while $d(N_{\nu_s} + N_{\bar{\nu}_s})/dt$ would be constant if the dynamical feedback were not taken into account. As we will discuss later, this may have important implications in the derivation of the sterile mass-mixing bounds.

4.3 Impact of the production of sterile particles on the lepton asymmetry

To gauge the overall impact of the radial and temporal growth of Y_{ν_τ} under various hydrodynamical conditions, we estimate the maximum value reached by $Y_{\nu_\tau}(r)$, $Y_{\nu_\tau}^{\text{max}}$, for the three benchmark time snapshots of the $18.6 M_\odot$ model. In order to do this, we compute $dY_{\nu_\tau}/dt(\Delta t = 0)$ and the stationary $Y_{\nu_\tau}^{\text{stat}}$ at different radii. The required time scale for Y_{ν_τ} to reach $Y_{\nu_\tau}^{\text{stat}}$ at each radius is

$$\Delta\tau(r) = \frac{Y_{\nu_\tau}^{\text{stat}}}{[dY_{\nu_\tau}/dt(\Delta t = 0)]}. \quad (4.2)$$

We then compute the maximum value of Y_{ν_τ} within Δt as follows:

$$Y_{\nu_\tau}^{\text{max}} = \begin{cases} Y_{\nu_\tau}^{\text{stat,max}} & \text{if } \Delta\tau_{\text{min}} \leq \Delta t, \\ Y_{\nu_\tau}^{\text{stat,max}} \times \frac{\Delta t}{\Delta\tau_{\text{min}}} & \text{if } \Delta\tau_{\text{min}} > \Delta t, \end{cases} \quad (4.3)$$

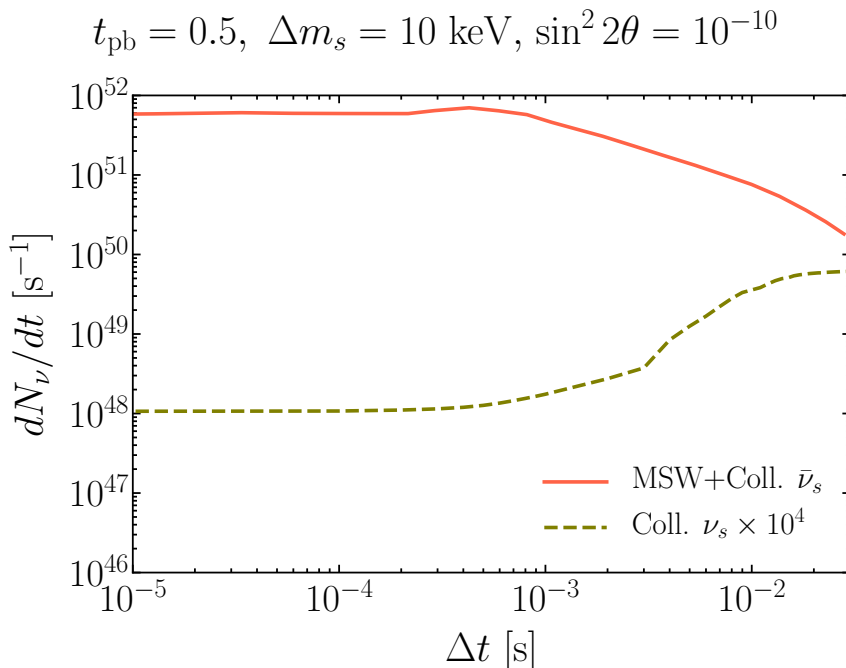


Figure 10. Time evolution of the total production rate of particles per unit time, dN_{ν_s}/dt (dashed, green line) and $dN_{\bar{\nu}_s}/dt$ (continuous, red line), produced up to the neutrinosphere radius ($R_\nu = 28 \text{ km}$) as a function of time for $t_{\text{pb}} = 0.5 \text{ s}$, $(\Delta m_s, \sin^2 2\theta) = (10 \text{ keV}, 10^{-10})$. As result of the dynamical feedback due to the production of sterile particles, the overall number of sterile (anti-)neutrinos is quenched after a certain Δt .

where $\Delta\tau_{\text{min}}$ is the minimum Δt required by Y_{ν_τ} to reach a stationary value, and $Y_{\nu_\tau}^{\text{stat,max}}$ is the maximum of $Y_{\nu_\tau}^{\text{stat}}$.

Figure 11 shows contour plots of the absolute maximum (as a function of r) of Y_{ν_τ} in the $(\Delta m_s, \sin^2 2\theta)$ plane for $\Delta t = 1 \text{ s}$ and for $t_{\text{pb}} = 0.05, 0.5$ and 1 s from left to right respectively. In order to guide the eye, the continuous lines are the isocontours of $Y_{\nu_\tau} = 0.01$ (black, dashed) and $Y_{\nu_\tau} = 0.1$ (black, solid), and $Y_{\nu_\tau} = 0.2$ (white, dot-dashed).

We adopt $\Delta t = 1 \text{ s}$, which is the typical cooling timescale for the SN core, for all three t_{pb} . This is an approximation since $\Delta t > 1 \text{ s}$ may be needed for Y_{ν_τ} to reach its stationary configuration depending on $(\Delta m_s, \sin^2 2\theta, t_{\text{pb}})$, but we see that a large range of the parameter space has $Y_{\nu_\tau}^{\text{max}} = Y_{\nu_\tau}^{\text{stat}} \simeq 0.2$ within 1 s . We also show the timescale $\Delta\tau$ corresponding to $Y_{\nu_\tau}^{\text{max}}$ in the bottom panel of Fig. 11. This figure clearly shows that, again, a significant portion of the parameter space has $\Delta\tau \lesssim 1 \text{ s}$. We note that although the contour shape is in qualitative agreement with Fig. 3 of Ref. [34], the values differ by orders of magnitude. In agreement with Fig. 3 of Ref. [34], we find that very small mixing angles require large Δt to approach the stationary solution. One can also see that smaller Δt are needed to achieve the stationary Y_{ν_τ} in a large region of the $(\Delta m_s, \sin^2 2\theta)$ parameter space as t_{pb} increases and larger values of Y_{ν_τ} are obtained. This is due to the fact that Y_e (and therefore V_{eff}) is smaller in the SN core as t_{pb} , allowing a wider range of energies to undergo MSW resonances.

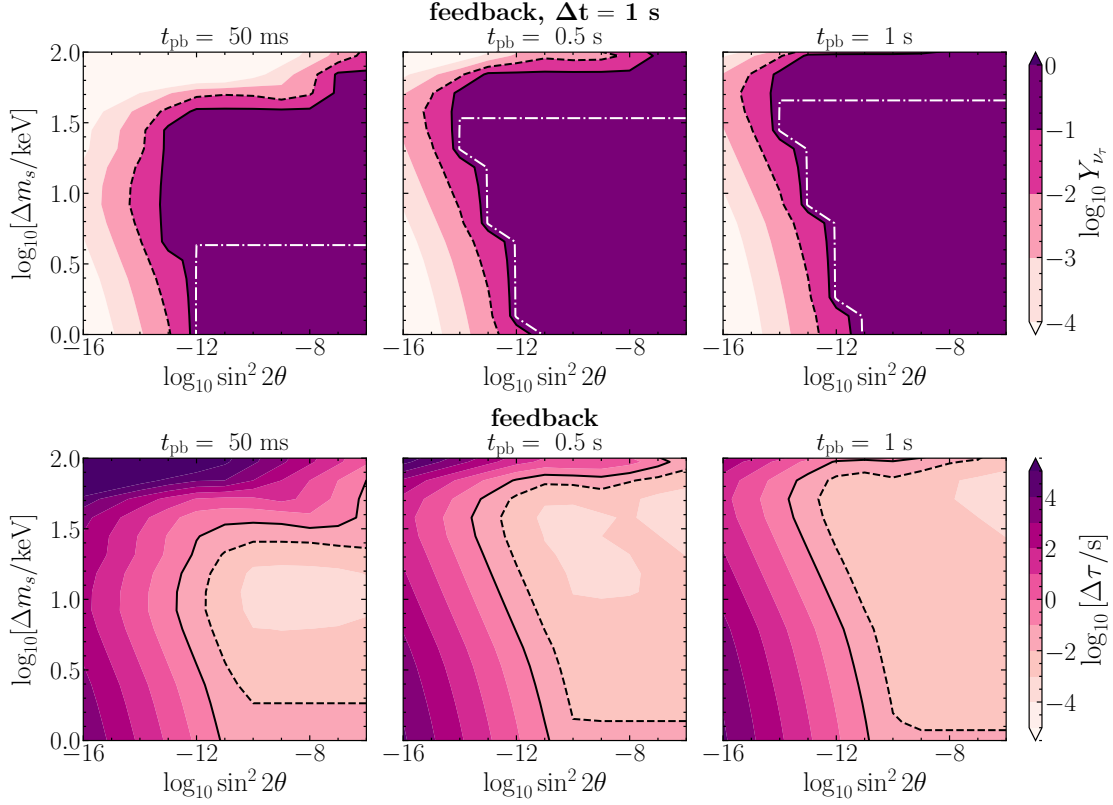


Figure 11. *Top:* Contour plots of the maximum of the radial profile of the stationary Y_{ν_τ} as a function of the mixing parameters $(\Delta m_s, \sin^2 2\theta)$ for $t_{\text{pb}} = 0.05, 0.5$ and 1 s (on the left, middle and right, respectively) obtained by including feedback effects within $\Delta t = 1$ s. The black lines indicate $Y_{\nu_\tau} > 0.01$ (dashed) and $Y_{\nu_\tau} > 0.1$ (solid); the white dash-dotted line marks $Y_{\nu_\tau} > 0.2$. *Bottom:* Contour plots of the time Δt required to reach the stationary Y_{ν_τ} (see text for details).

4.4 Impact of the production of sterile particles on the chemical potential

Besides affecting the effective potential V_{eff} , the generation of Y_{ν_τ} due to the production of sterile neutrinos leads to the growth of ν_τ chemical potential μ_{ν_τ} , which can further suppress the sterile neutrino production. We compute the evolution of μ_{ν_τ} , for fixed t_{pb} , by finding the root of

$$Y_{\nu_\tau}(r) - \frac{1}{n_B(r)} \sum_{k=1}^L \left(\frac{dn_{\nu_\tau}}{dE_k}(r, \mu_{\nu_\tau}) - \frac{dn_{\bar{\nu}_\tau}}{dE_k}(r, -\mu_{\nu_\tau}) \right) \Delta E_k = 0, \quad (4.4)$$

with $[E_{k=1}, E_{k=L}] = [E_{\text{min}}, E_{\text{max}}]$.

Figure 12 shows the temporal evolution of Y_{ν_τ} , μ_{ν_τ} and V_{eff} for $(\Delta m_s, \sin^2 2\theta) = (10 \text{ keV}, 10^{-10})$. One can notice that Y_{ν_τ} computed by including the feedback on μ_{ν_τ} is considerably smaller than the one calculated without any feedback. Additionally, due to the decrease of the tau neutrino number density determined by the growth of μ_{ν_τ} , the stationary value $Y_{\nu_\tau}^{\text{stat}}$ is not reached within 1 s, as it was in the simulations with feedback on V_{eff} but without feedback on μ_{ν_τ} , see Fig. 7 for comparison. When the feedback on μ_{ν_τ} is included, the timescale necessary for reaching the final saturated value is much longer than in the case with feedback on V_{eff} only ($\Delta t \sim 0.17$ s vs. $\Delta t \sim 0.03$ s), see Fig. 7 for comparison.

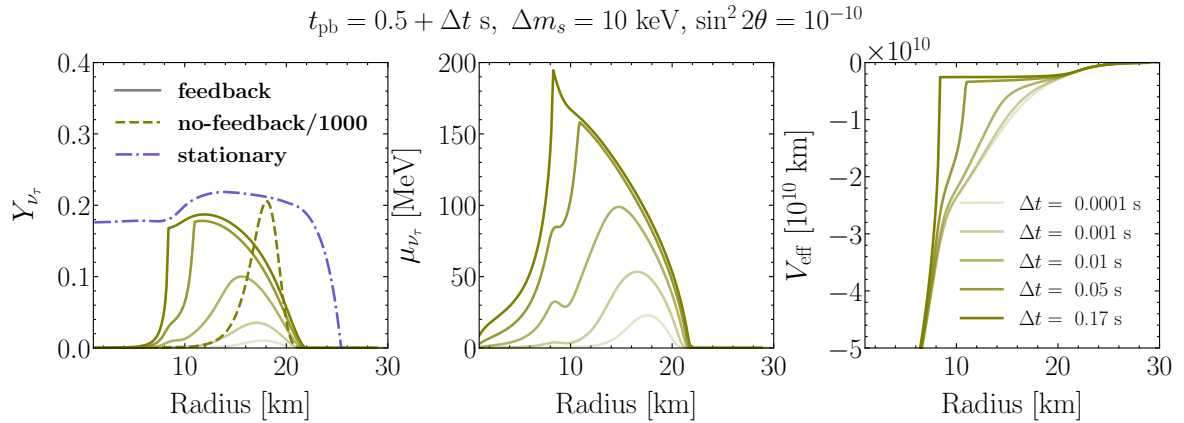


Figure 12. *Left:* Radial profile of Y_{ν_τ} for the case with feedback on Y_{ν_τ} and μ_{ν_τ} for $t_{\text{pb}} = 0.5$ s, $(\Delta m_s, \sin^2 2\theta) = (10 \text{ keV}, 10^{-10})$, and $\Delta t = 0.17$ s. The dashed line represents the case without feedback ($\Delta t = 0$), the continuous lines with different hues mark the temporal evolution for the case with feedback due to the production of sterile particles. The dot-dashed line shows $Y_{\nu_\tau}^{\text{stat}}$ for $E_{\text{max}} = 1000$ MeV (see text for details). *Middle:* Radial evolution of μ_{ν_τ} for the case with feedback. *Right:* Radial profile of V_{eff} . The dynamical feedback due to flavor conversions in sterile states leads to a considerable production of μ_{ν_τ} .

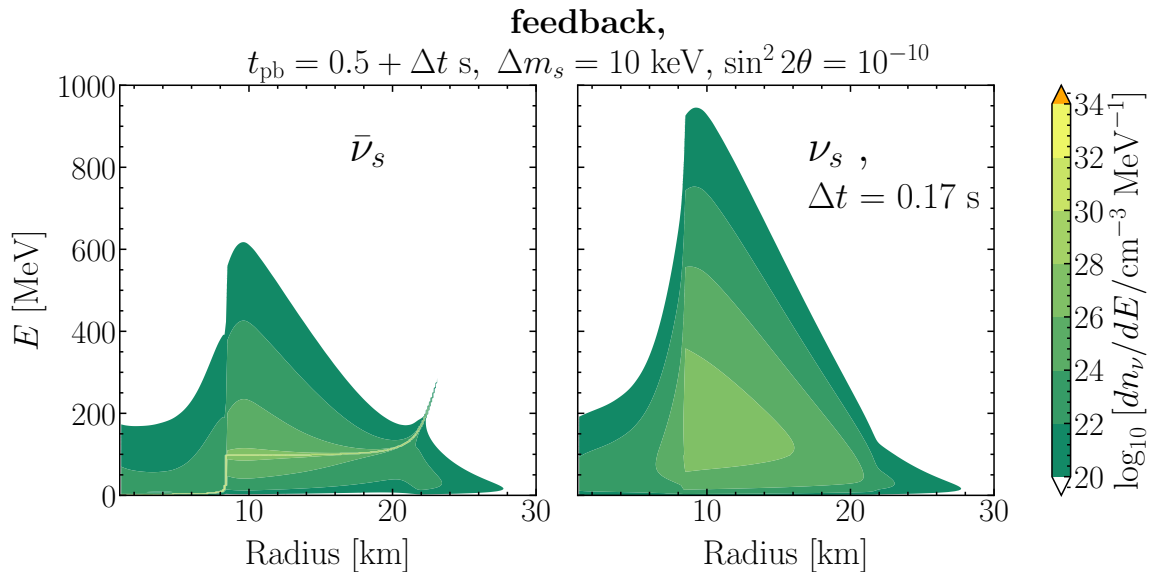


Figure 13. Contour plots of the number density of $\bar{\nu}_s$'s (left panel) and ν_s 's (right panel) per unit energy in the plane spanned by the distance from the SN core and the neutrino energy for $(\Delta m_s, \sin^2 2\theta) = (10 \text{ keV}, 10^{-10})$, $t_{\text{pb}} = 0.5$ s, and $\Delta t = 0.17$ s with dynamical feedback effect due to the production of sterile particles on V_{eff} and μ_{ν_τ} . See Fig. 8 for comparison with cases without the feedback ($\Delta t = 0$ s) and with feedback only on V_{eff} .

Figure 13 shows contour plots of the sterile antineutrino (on the left) and neutrino (on the right) number densities as a function of energy and SN radius for $\Delta t = 0.17$ s, and with feedback on μ_{ν_τ} and V_{eff} . By comparing Figs. 13 and 8, one can notice that the resonance energy does not grow as high as in the case without the feedback on the neutrino

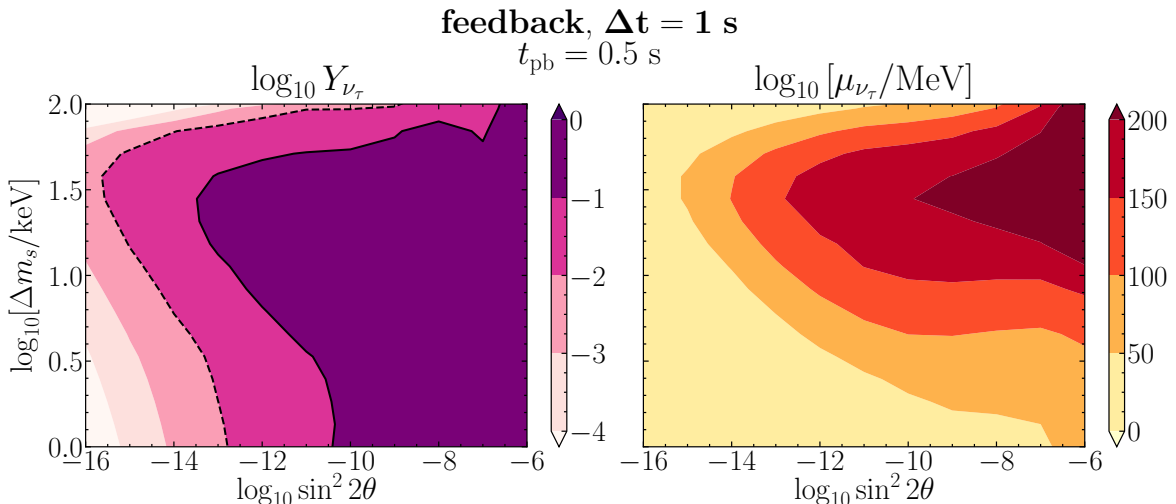


Figure 14. *Left:* Contour plot of the maximum of the radial profile of Y_{ν_τ} as a function of the mixing parameters (Δm_s , $\sin^2 2\theta$) for $t_{\text{pb}} = 0.5$ s obtained by including feedback effects on the effective matter potential and of the chemical potential on the neutrino energy distributions within $\Delta t = 1$ s. The black lines indicate $Y_{\nu_\tau} > 0.01$ (dashed) and $Y_{\nu_\tau} > 0.1$ (solid). *Right:* Contour plot of μ_{ν_τ} corresponding to the maximum of Y_{ν_τ} . The production of sterile neutrinos leads to the generation of a non-negligible μ_{ν_τ} , which in turn has an impact on Y_{ν_τ} and $n_{\bar{\nu}_\tau}$, n_{ν_τ} .

energy distributions. With the increase of the chemical potential, the number density of $\bar{\nu}_\tau$ decreases. It results in smaller Y_{ν_τ} , as fewer antineutrinos can convert into sterile states. This leads to a smaller V_{eff} and less energetic neutrinos undergo resonances at the same radius. On the other hand, the number density of neutrinos increases due to the non-zero chemical potential. The results of the the cumulative luminosity of sterile neutrinos and total production rate of sterile particles per unit time are qualitatively similar to those presented in Figs. 9 and 10 when including the chemical potential feedback.

To investigate the impact of the feedback of $\mu_{\nu_\tau} \neq 0$ on the neutrino energy distributions and therefore on flavor conversions, we estimate the maximum value reached by Y_{ν_τ} and the corresponding μ_{ν_τ} in the ($\Delta m_s, \sin^2 2\theta$) plane for $t_{\text{pb}} = 0.5$ s and $\Delta t = 1$ s. By comparing the contour plot of Y_{ν_τ} in Fig. 14 with the one in the top middle panel of Fig. 11, one can see that the overall trend remains unchanged, but the maximum Y_{ν_τ} can vary within 10%. In particular, the region with $Y_{\nu_\tau} > 0.1$ shrunk; in that same region, a non-negligible μ_{ν_τ} is also produced.

4.5 Discussion

The alteration of the neutrino lepton number due to the production of keV-mass sterile neutrinos was first discussed in Refs. [30, 31, 34] in the context of a one-zone model (although Ref. [31] investigated the e - s mixing instead of the τ - s one). Also Ref. [32] studies the role of τ - s mixing, but without considering the feedback effects on the hydrodynamical quantities.

Reference [34] adopted a one-zone model with homogeneous and isotropic core, and with constant temperature and baryon density. Their Fig. 3 estimates the time required by the system to converge towards a stationary Y_{ν_τ} ; despite our modeling is more sophisticated, the bottom panel of our Fig. 11 is in qualitative agreement with Fig. 3 of [34]; we find that $Y_{\nu_\tau}^{\text{stat}}$ is reached within a much smaller Δt .

Reference [33] attempts to couple the active-sterile neutrino flavor conversion physics to the hydrodynamical simulation by assuming adiabatic flavor conversions. In Ref. [33], it is concluded that the mixing with ν_τ 's does not significantly alter the explosion physics and has no observable effect on the neutrino luminosities at early times. This is at odds with our results that include a detailed modeling of the neutrino microphysics, see bottom panel of Fig. 11. Most importantly, as shown in Figs. 5, 6 and 9, the adiabaticity of the flavor conversions strongly depends on the mixing parameters, and the collisionally enhanced production of sterile particles is non-negligible.

As highlighted in Figs. 10 and 12 (see also the left panel of Fig. 7), tracking the evolution of Y_{ν_τ} and μ_{ν_τ} in time and radius self-consistently is important in order to derive robust constraints on the allowed $(\Delta m_s, \sin^2 2\theta)$ parameter space. Although we only investigate the sterile neutrino production on a static SN background, our results hint towards more robust bounds in the mass-mixing parameter space of sterile neutrinos with respect to the ones currently reported in the literature, if a self-consistent modeling of the sterile neutrino physics is included.

In order to give an idea of how existing bounds on sterile neutrino mass-mixing parameters would be modified, if a self-consistent estimation of the feedback effects were implemented, we estimate the total energy emitted in sterile neutrinos and antineutrinos:

$$E_{\nu_s}(\Delta t) = \sum_{\nu, \bar{\nu}} \sum_{y=1}^N \sum_{j=1}^M \sum_{k=1}^L \Delta t_y \Delta r'_j \Delta E_k E_k 4\pi r_j'^2 P_{\tau s}(E_{\text{res}}, r'_j, t_y) \frac{dn_{\nu_\tau, \bar{\nu}_\tau}(r'_j, t_y)}{dE_k} \frac{1}{\Delta r'_j}, \quad (4.5)$$

where $[t_{y=1}, t_{y=N}] = [t_{\text{pb}}, t_{\text{pb}} + \Delta t]$, $[r'_{j=1}, r'_{j=M}] = [1 \text{ km}, R_\nu]$, $[E_{k=1}, E_{k=L}] = [E_{\text{min}}, E_{\text{max}}]$, $P_{\tau s}$ is the conversion probability due to the MSW effect (Eq. 3.6) or collisions (Eq. 3.9), and $dn_{\nu_\tau, \bar{\nu}_\tau}/dE$ has been estimated by including μ_{ν_τ} due to the generation of sterile particles. The time interval $\Delta t = 1 \text{ s}$ has been considered as representative of the characteristic timescale of the SN neutrino emission during the proto-neutron star cooling. We then compare $E_{\nu_s}(\Delta t)$ to the typical binding energy of a neutron star, $E_B = 3 \times 10^{53} \text{ ergs}$. Note that this comparison only provides a conservative estimate of the excluded mass-mixing parameter space of sterile neutrinos. A robust bound can only be placed through a self-consistent assessment, including the dynamical feedback effects of flavor conversions in time-dependent hydrodynamical SN simulations.

Figure 15 shows the contours of E_{ν_s}/E_B for $\Delta t = 1 \text{ s}$, $t_{\text{pb}} = 0.5 \text{ s}$ for the case without feedback (left panel) and with feedback on μ_{ν_τ} and Y_{ν_τ} due to the production of sterile neutrinos (right panel)². One can easily notice that the inclusion of the dynamical feedback due to the production of sterile particles significantly affects the “excluded” region ($E_{\nu_s}/E_B > 1$). In particular, the feedback effects seem to lead to larger region of the parameter space to be still compatible with SNe.

5 Outlook

Sterile neutrinos with keV mass have the potential to dramatically affect the supernova physics generating a large neutrino lepton asymmetry. This work constitutes a step for-

²For very large mixing angles ($\sin^2 2\theta > 10^{-10}$), the computational time needed to estimate the feedback effects due to the production of sterile particles increases dramatically. Hence, the final values of μ_{ν_τ} , Y_{ν_τ} , $E_{\nu_s}(\Delta t)$ for those mixing angles have been extrapolated by a power-law. By comparison with smaller mixing angles where the runs are done for $\Delta t = 1 \text{ s}$, we estimate that our approximation leads to an error of a few % at most.

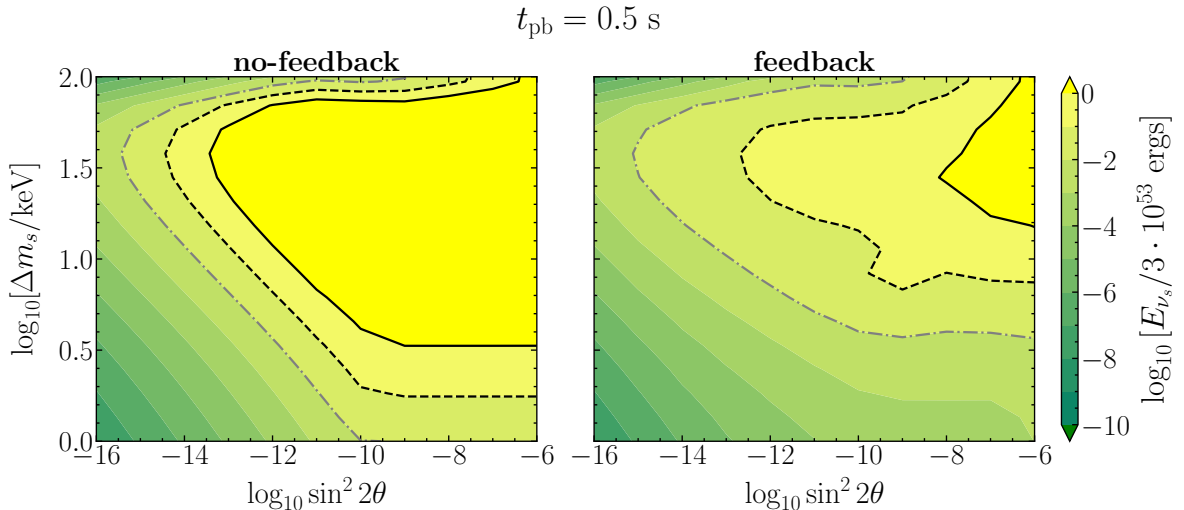


Figure 15. Ratio of energy emitted in sterile (anti-)neutrinos over $\Delta t = 1 \text{ s}$ for $t_{\text{pb}} = 0.5 \text{ s}$ without feedback (left panel) and with the feedback (right panel) to the benchmark gravitational energy (E_{ν_s}/E_B with $E_B = 3 \times 10^{53} \text{ ergs}$). The grey, dash-dotted line indicates $E_{\nu_s}/E_B > 0.01$, the black dashed line stands for $E_{\nu_s}/E_B > 0.1$; the black solid line marks the excluded region, where the energy ratio $E_{\nu_s}/E_B > 1$. Although robust bounds on $(\sin^2 2\theta, \Delta m_s)$ can be derived through a self-consistent and time-dependent estimation of the production of sterile particles only, the dynamical feedback due to flavor conversions in sterile states considerably relaxes the excluded region of the parameter space of sterile neutrinos.

ward towards a self-consistent, radial and time-dependent modeling of the keV-mass sterile neutrino production and propagation in the supernova core.

We develop the first self-consistent treatment of active–sterile flavor conversions, by employing stationary, but radially evolving profiles for the hydrodynamical quantities of interest. We model the neutrino flavor evolution in the presence of collisions in the SN core by assuming spherical symmetry and explore the development of the $\nu_\tau\text{--}\bar{\nu}_\tau$ lepton asymmetry in radius and time as a function of $(\Delta m_s, \sin^2 2\theta)$. Given the complications induced by the modeling of active–sterile conversions at nuclear densities, we work in a two flavor framework and only consider the mixing in the (ν_τ, ν_s) sector.

The production of sterile particles with $\mathcal{O}(1 - 100) \text{ keV}$ mass, through the $\bar{\nu}_\tau\text{--}\bar{\nu}_s$ MSW resonant conversions and resonantly enhanced collisions, leads to the development of a $\nu_\tau\text{--}\bar{\nu}_\tau$ lepton asymmetry. The dynamical feedback induced on the effective matter background experienced by neutrinos is strongly affected by the production of sterile particles and is responsible for the growth in time of the $\nu_\tau\text{--}\bar{\nu}_\tau$ asymmetry, which in turn affects the (anti)neutrino energy distributions through a related non-zero chemical potential.

A scan of the mass and mixing parameter space for sterile neutrinos highlights that the potential feedback of the sterile neutrino mixing on the ν_τ lepton asymmetry can be larger than 0.15. This is largely overestimated when the feedback effects are not included and would drastically affect the supernova bounds on the mass-mixing of sterile neutrinos.

The generation of a large ν_τ asymmetry in the supernova core may have relevant implications for the post-bounce evolution of the proto-neutron star. For example, the average temperature of the active neutrinos in the accretion and early cooling phase may be higher due to the faster cooling of the proto-neutron star and, in turn, this may affect the neutrino

heating within a self-consistent time-dependent hydrodynamical framework. Likewise, the nucleosynthesis conditions in the neutrino-driven wind may be affected. Note that similar conclusions would also hold in the case of ν_μ - ν_s mixing, and this may also affect the explosion mechanism substantially [45].

Another observational consequence connected to the generation of sterile neutrinos with keV-mass is that the energy distributions of the active neutrinos detected on Earth will be modified. In particular, we neglect the mixing of active neutrinos of different flavors among themselves, but the production of sterile neutrinos from the τ channel will of course indirectly affect the the other active sectors.

In conclusions, sterile neutrinos with keV mass can have a major impact on the supernova physics. Our work highlights the important implications of a self-consistent modeling of the related microphysics in order to explore the consequences of non-standard physics occurring in the core of a massive star. Only through a self-consistent modeling of the production of sterile particles, one would be able to extrapolate robust constraints on the mass and mixing parameters of these sterile and weakly-interacting particles.

Acknowledgments

We are grateful to Chris Pethick and Georg Raffelt for insightful discussions. We are also grateful to Robert Bollig and Thomas Janka for granting access to the data of the supernova model adopted in this work. IT acknowledges support from the Villum Foundation (Project No. 13164), the Knud Højgaard Foundation, and the Deutsche Forschungsgemeinschaft through Sonderforschungsbereich SFB 1258 “Neutrinos and Dark Matter in Astro- and Particle Physics” (NDM). MRW acknowledges support from the Ministry of Science and Technology, Taiwan under Grant No. 107-2119-M-001-038 and No. 108-2112-M-001 -010.

A Neutrino interaction rates

Neutrinos interact within the dense SN core. For a given interaction, not all the phase space of the outgoing particles may be available due to Pauli blocking effects. In this Appendix, in order to single out the main neutrino interaction rates contributing to the total rate Γ_ν (see Eq. 3.11), we estimate the reaction rates involving ν_τ ’s and $\bar{\nu}_\tau$ ’s for our three selected post-bounce times ($t_{\text{pb}} = 0.05, 0.5$ and 1 s) in the absence of flavor conversions. We will also provide an assessment of the Pauli blocking effects of nucleons. An average over the neutrino energy distribution will be considered in order to have an overall picture of the most relevant processes.

The main reactions occurring in the SN core should involve the scattering of neutrinos on nucleons (i.e., $p + \nu_\tau \rightarrow p + \nu_\tau$ and $n + \nu_\tau \rightarrow n + \nu_\tau$):

$$\Gamma(p + \nu_\tau \rightarrow p + \nu_\tau) = Y_e n_B \frac{\int dE \sigma_{\nu p}(E) dn_{\nu_\tau}/dE}{n_{\nu_\tau}}, \quad (\text{A.1})$$

$$\Gamma(n + \nu_\tau \rightarrow n + \nu_\tau) = (1 - Y_e) n_B \frac{\int dE \sigma_{\nu n}(E) dn_{\nu_\tau}/dE}{n_{\nu_\tau}}, \quad (\text{A.2})$$

where the cross sections, $\sigma_{\nu n}$ and $\sigma_{\nu p}$, are defined as from Ref. [46], dn_ν/dE is the neutrino energy distribution introduced in Sec. 2, Y_e is the electron fraction, n_B the local baryon density, and T the medium temperature.

The other interaction rates are derived following Ref. [47], which estimated the contributions to Γ_ν by thermally averaging the energy-dependent interaction rate on the neutrino Fermi-Dirac distribution, closely. The neutral current (NC) scattering of neutrinos among themselves is governed by the following rates

$$\Gamma(\nu_\tau \bar{\nu}_\tau \rightarrow \nu_e \bar{\nu}_e) = \frac{4}{\pi^3} G_F^2 T^5, \quad (\text{A.3})$$

and

$$\Gamma(\nu_\tau \nu_e \rightarrow \nu_\tau \nu_e, \nu_\tau \bar{\nu}_e \rightarrow \nu_\tau \bar{\nu}_e) = 4\Gamma(\nu_x \bar{\nu}_\tau \rightarrow \nu_e \bar{\nu}_e) = \frac{16}{\pi^3} G_F^2 T^5. \quad (\text{A.4})$$

The ν - ν scattering leading to e^+e^- pair production has instead an interaction rate defined as

$$\Gamma(\nu_\tau \bar{\nu}_\tau \rightarrow e^+ e^-) = \Gamma(\nu_\tau \bar{\nu}_\tau \rightarrow \nu_e \bar{\nu}_e) (C_{V,e}^2 + C_{A,e}^2) \eta_e^4 e^{-\eta_e} / 12, \quad (\text{A.5})$$

where $\eta_e = \mu_e/T$ is the degeneracy parameter and $C_{V,e}(C_{A,e}) = 1/2(-1/2 + 2\sin^2 \theta_W)$ is the vector (axial) coupling constant with $\sin^2 \theta_W = 0.23$. The related interaction rate for $\nu_\tau e^- \rightarrow \nu_\tau e^-$ is

$$\Gamma(\nu_\tau e^- \rightarrow \nu_\tau e^-) = \Gamma(\nu_\tau \bar{\nu}_\tau \rightarrow \nu_e \bar{\nu}_e) (C_{V,e}^2 + C_{A,e}^2) 3\eta_e^2. \quad (\text{A.6})$$

The thermally averaged rate for the Bremsstrahlung processes $\nu_\tau \bar{\nu}_\tau NN \rightarrow NN$ is:

$$\Gamma(\nu_\tau \bar{\nu}_\tau nn \rightarrow nn) = \frac{3C_A^2 G_F^2}{\pi} (1 - Y_e) n_B T^2 \frac{\Gamma_\sigma/T}{20\pi} \xi, \quad (\text{A.7})$$

and

$$\Gamma(\nu_\tau \bar{\nu}_\tau pp \rightarrow pp) = \frac{3C_A^2 G_F^2}{\pi} Y_e n_B T^2 \frac{\Gamma_\sigma/T}{20\pi} \xi. \quad (\text{A.8})$$

In the two Bremsstrahlung rates introduced above, ξ is the dimensionless mean free path and it has been assumed to be 1 for simplicity [47]. The spin fluctuation rate (Γ_σ) is given by

$$\Gamma_\sigma = \frac{8\sqrt{2}\pi\alpha_\pi^2}{3\pi^2} \eta_*^{3/2} \frac{T^2}{m_N}, \quad (\text{A.9})$$

where $\eta_* = p_F^2/(2m_N T)$ is the degeneracy parameter for the nucleons, $p_F = \sqrt{2m_N \mu_N}$ the Fermi momentum of nucleons with m_N their mass, and $\alpha_\pi = (f^2 m_N / m_\pi)^2 / 4\pi \approx 15$ with $f \approx 1$.

Figure 16 shows the neutrino interaction rates introduced above averaged over the neutrino energy distribution as a function of the distance from the SN core. The different panels correspond to $t_{\text{pb}} = 0.05, 0.5$ and 1 s from left to right, respectively. The various reaction rates have been plotted with different colors as indicated in the legend. The NC scatterings of neutrinos on nucleons, $p + \nu_\tau \rightarrow p + \nu_\tau$ and $n + \nu_\tau \rightarrow n + \nu_\tau$, provide the main contribution to the total neutrino reaction rate Γ_ν followed by the ν scattering on electrons. Notably since the ν - e scattering should mainly contribute in the proximity of the neutrino decoupling radius (i.e., when neutrinos are free-streaming) and all others rates are sub-leading, we only include the energy-dependent reaction rates $N + \nu_\tau \rightarrow N + \nu_\tau$ in the estimation of the sterile neutrino collisional production. Moreover, we assume that the scattering on nucleons is elastic up to $E_{\text{max}} = 1000$ MeV. In fact, as discussed in Sec. 4, the contribution to the sterile production coming from collisions for neutrino energies above 400–500 MeV is only relevant for very high masses of sterile neutrinos (above 100 keV).

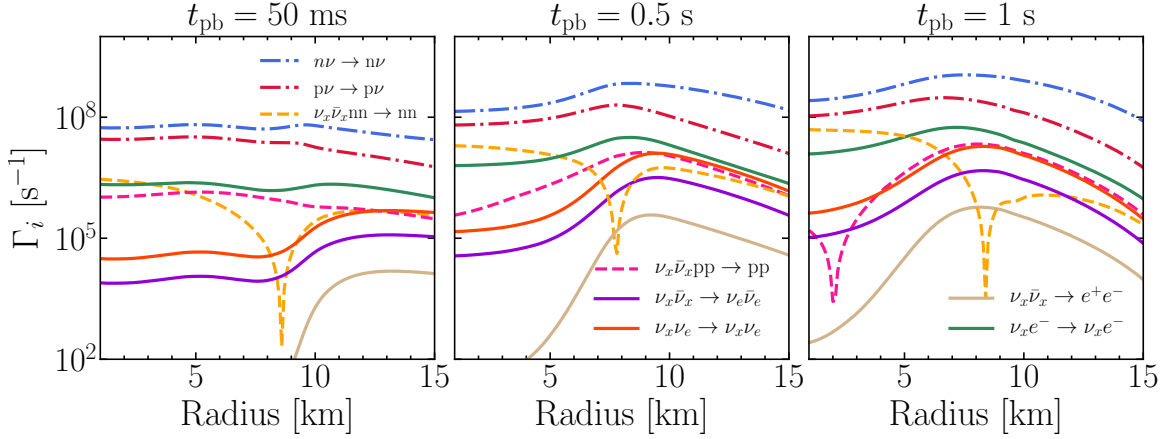


Figure 16. Neutrino interaction rates averaged on the neutrino energy distribution as a function of the distance from the SN core for $t_{\text{pb}} = 0.05, 0.5$ and 1 s (from left to right, respectively). The dominant interaction channels are the NC ν - N scatterings for all post-bounce times. The dips present below ~ 10 km, in the $\nu_\tau \bar{\nu}_\tau nn \rightarrow nn$ lines come from μ_n crossing zero.

In the dense SN core, for a given reaction, not all final states are allowed because of Pauli blocking effects [48, 49]. In fact, the Pauli blocking forbids the scattering of fermions into occupied states, leading to a suppression of the neutrino interaction rate. In the following, for the sake of simplicity, we assume that the distribution function of nucleons does not change as a result of the scattering of nucleons on neutrinos (i.e., $E_\nu \ll m_N$). This assumption leads to a simplified estimation of the Pauli blocking factor of nucleons that suits well our purposes. In the derivation of the Pauli blocking effects, we closely follow Refs. [48, 50] and focus on the main reaction $N + \nu_\tau \rightarrow N + \nu_\tau$:

$$F_{\nu,N}(E) = (1 - f(E)) \int_0^\infty \frac{2}{2\pi^2 n_N} dp_N p_N^2 f(E_N) [1 - f(E_N)] , \quad (\text{A.10})$$

where $E_N = \sqrt{p_N^2 + m_N^2} + U_\star$ is the nucleon energy, with p_N the nucleon momentum, m_N the effective nucleon mass, U_\star the nucleon mean field potential, and $f(E_i)$ is the Fermi-Dirac energy distribution.

Figure 17 shows the radial dependence of $F_{\nu,N}(E)$ averaged over the neutrino energy distribution for $t_{\text{pb}} = 0.05, 0.5$ and 1 s from left to right, respectively. Notably the Pauli blocking effect is slightly larger for the ν - n channel. Moreover, $\langle F_{\nu,N}(E) \rangle \rightarrow 1$ as neutrinos approach the decoupling radius, as expected.

The Pauli blocking factor $F_{\nu,N}(E)$ modifies the total collision rate of neutrinos and antineutrinos³. The overall interaction rate is then defined as:

$$\Gamma_{\nu_\tau}(E) = F_{\nu,p}(E)\sigma_{\nu,p}(E)Y_p + F_{\nu,n}(E)\sigma_{\nu,n}(E)Y_n , \quad (\text{A.11})$$

with $Y_p = Y_e$ ($Y_n = 1 - Y_p$) the proton (neutron) fraction.

³Notably, the collision rate will be modified in a different way for neutrinos and antineutrinos, if they have a non-zero chemical potential as ν_e and $\bar{\nu}_e$. In fact, the Fermi-Dirac distribution depends on the neutrino chemical potential, and $\mu_\nu = -\mu_{\bar{\nu}}$.

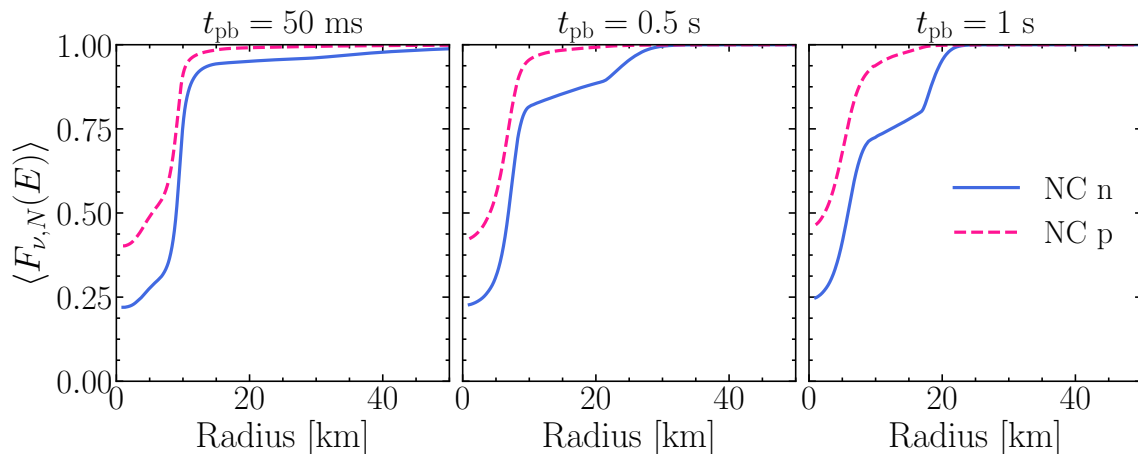


Figure 17. Pauli blocking factor of nucleons averaged over the neutrino energy distribution for the NC scattering of ν_τ and $\bar{\nu}_\tau$ as a function of the distance from the SN core for $t_{\text{pb}} = 0.05, 0.5$ and 1 s (from left to right, respectively). The Pauli blocking effects are larger for ν - n interactions. The Pauli blocking becomes negligible in the proximity of the neutrino decoupling region.

B Neutrino conversions in the trapping regime

In the SN core, neutrinos are trapped and sterile particles can be produced because of collisions, as illustrated in Sec. 3.2. Within each SN shell of width Δr_{step} , neutrinos may undergo multiple collisions if $\lambda_\nu \ll \Delta r_{\text{step}}$ as illustrated in Fig. 18. As a consequence, we estimate the overall production of sterile neutrinos through each SN shell by adopting a recursive method.

For the sake of simplicity, we assume that the number density of neutrinos is constant through the each SN shell of width Δr_{step} . This is a reasonable assumption given that $\Delta r_{\text{step}} \simeq \mathcal{O}(10^{-2} - 10^{-1})$ km. We can then sub-divide Δr_{step} in multiple sub-shells each of width $\lambda_\nu \ll \Delta r_{\text{step}}$ as shown in Fig. 18.

If no sterile neutrinos are present in the first sub-shell, then the number density of sterile particles produced in the first sub-shell of width λ_ν for a fixed energy E is

$$n_{\nu_s}^{(1)} = n_{\nu_\tau}^{(0)} \langle P_{\tau s} \rangle, \quad (\text{B.1})$$

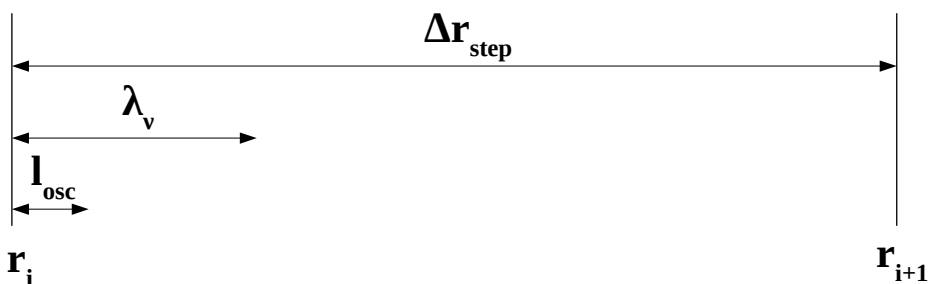


Figure 18. Diagram representing a comparison among Δr_{step} , λ_ν , and l_{osc} within one SN shell. Multiple collisions occur within one SN shell. Notice that the diagram is not in scale. For example, deep inside the SN core for $r \sim 5$ km, $(\Delta m_s, \sin^2 2\theta) = (10 \text{ keV}, 10^{-6})$, and neutrino energy $E = 100$ MeV, we have $l_{\text{osc}} \sim 10^{-10}$ km, $\lambda_\nu \sim 10^{-4}$ km, and $\Delta r_{\text{step}} = 0.1$ km.

with $\langle P_{\tau s} \rangle$ defined as in Eq. 3.9 and $n_{\nu_\tau}^0$ denoting the density of ν_τ at the beginning of the first SN sub-shell.

Similarly, in the second sub-shell of width λ_ν , the number density of sterile particles is

$$n_s^{(2)} = n_{\nu_\tau}^{(1)} \langle P_{\tau s} \rangle + n_{\nu_s}^{(1)} (1 - \sin^2 2\tilde{\theta} \langle P_{\tau s} \rangle) , \quad (\text{B.2})$$

where $\tilde{\theta}$ is the mixing angle in matter assuming a constant matter potential within λ_ν , and it is defined as $\sin^2 2\tilde{\theta} = 4 \langle P_{\tau s}(E, r) \rangle$. The term $(1 - \sin^2 2\tilde{\theta} \langle P_{\tau s} \rangle)$ accounts for a possibility of reconversion of sterile neutrinos in active ones; $n_{\nu_\tau}^{(1)} \approx n_{\nu_\tau}^{(0)}$ due to the assumption that the active neutrinos are trapped and their number density within one SN shell is constant. At the end of the SN shell of width Δr_{step} , the number density of sterile particles is

$$n_{\nu_s}^{(n)} = \sum_{k=1}^{k=n} n_{\nu_\tau}^{(0)} \langle P_{\tau s} \rangle (1 - \sin^2 2\tilde{\theta} \langle P_{\tau s} \rangle)^{k-1} . \quad (\text{B.3})$$

The overall conversion factor within a SN shell of width Δr_{step} is then

$$P_{\tau s}(n) = \sum_{k=1}^{k=n} \langle P_{\tau s} \rangle (1 - \sin^2 2\tilde{\theta} \langle P_{\tau s} \rangle)^{k-1} . \quad (\text{B.4})$$

The effective conversion probability follows from Eq. B.4:

$$P_{\tau s}(E, n) = \frac{1}{n} \sum_{k=1}^n \langle P_{\tau s} \rangle (1 - \sin^2 2\tilde{\theta} \langle P_{\tau s} \rangle)^{k-1} = \frac{1 - (1 - \sin^2 2\tilde{\theta} \langle P_{\tau s} \rangle)^n}{n \langle P_{\tau s} \rangle} . \quad (\text{B.5})$$

The energy distribution of sterile (anti-)neutrinos produced through collisions until the ν_τ neutrinosphere radius is

$$\left(\frac{d\mathcal{N}}{dEdt} \right)_{s, \text{coll}} = \sum_{i=1}^N \Delta V_i \frac{dn_{\nu_\tau}}{dE}(r'_i) P_{\tau s}(E, n, r'_i) \Gamma_\nu(r'_i) \quad (\text{B.6})$$

with $\Delta V_i = 4\pi r_i'^2 \Delta r_{\text{step}, i}$; this is equivalent to

$$\left(\frac{d\mathcal{N}}{dEdt} \right)_{s, \text{coll}} = \sum_{i=1}^N \Delta V_i \frac{dn_{\nu_\tau}}{dE}(r'_i) n P_{\tau s}(E, n, r'_i) \Delta r_{\text{step}, i}^{-1} . \quad (\text{B.7})$$

References

- [1] A. Mirizzi, I. Tamborra, H.-T. Janka, N. Saviano, K. Scholberg, R. Bollig et al., *Supernova Neutrinos: Production, Oscillations and Detection*, *Riv. Nuovo Cim.* **39** (2016) 1–112, [[1508.00785](#)].
- [2] H.-T. Janka, *Explosion Mechanisms of Core-Collapse Supernovae*, *Ann. Rev. Nucl. Part. Sci.* **62** (2012) 407–451, [[1206.2503](#)].
- [3] H.-T. Janka, *Neutrino-Driven Explosions*, *Handbook of Supernovae*, p. 1095. 2017. [[1702.08825](#)].
- [4] K. Kotake, K. Sumiyoshi, S. Yamada, T. Takiwaki, T. Kuroda, Y. Suwa et al., *Core-Collapse Supernovae as Supercomputing Science: a status report toward 6D simulations with exact Boltzmann neutrino transport in full general relativity*, *PTEP* **2012** (2012) 01A301, [[1205.6284](#)].

- [5] A. Burrows, *Colloquium: Perspectives on core-collapse supernova theory*, *Rev. Mod. Phys.* **85** (2013) 245, [[1210.4921](#)].
- [6] S. Chakraborty, R. Hansen, I. Izaguirre and G. G. Raffelt, *Collective neutrino flavor conversion: Recent developments*, *Nucl. Phys.* **B908** (2016) 366–381, [[1602.02766](#)].
- [7] B. Dasgupta, E. P. O’Connor and C. D. Ott, *The Role of Collective Neutrino Flavor Oscillations in Core-Collapse Supernova Shock Revival*, *Phys. Rev.* **D85** (2012) 065008, [[1106.1167](#)].
- [8] E. O’Connor et al., *Global Comparison of Core-Collapse Supernova Simulations in Spherical Symmetry*, *J. Phys.* **G45** (2018) 104001, [[1806.04175](#)].
- [9] H.-T. Janka, T. Melson and A. Summa, *Physics of Core-Collapse Supernovae in Three Dimensions: a Sneak Preview*, *Ann. Rev. Nucl. Part. Sci.* **66** (2016) 341–375, [[1602.05576](#)].
- [10] R. F. Sawyer, *Neutrino cloud instabilities just above the neutrino sphere of a supernova*, *Phys. Rev. Lett.* **116** (2016) 081101, [[1509.03323](#)].
- [11] R. F. Sawyer, *The multi-angle instability in dense neutrino systems*, *Phys. Rev.* **D79** (2009) 105003, [[0803.4319](#)].
- [12] I. Izaguirre, G. G. Raffelt and I. Tamborra, *Fast Pairwise Conversion of Supernova Neutrinos: A Dispersion-Relation Approach*, *Phys. Rev. Lett.* **118** (2017) 021101, [[1610.01612](#)].
- [13] S. Abbar and M. C. Volpe, *On Fast Neutrino Flavor Conversion Modes in the Nonlinear Regime*, *Phys. Lett.* **B790** (2019) 545–550, [[1811.04215](#)].
- [14] B. Dasgupta, A. Mirizzi and M. Sen, *Fast neutrino flavor conversions near the supernova core with realistic flavor-dependent angular distributions*, *JCAP* **1702** (2017) 019, [[1609.00528](#)].
- [15] F. Capozzi, B. Dasgupta, A. Mirizzi, M. Sen and G. Sigl, *Collisional triggering of fast flavor conversions of supernova neutrinos*, *Phys. Rev. Lett.* **122** (2019) 091101, [[1808.06618](#)].
- [16] S. A. Richers, G. C. McLaughlin, J. P. Kneller and A. Vlasenko, *Neutrino Quantum Kinetics in Compact Objects*, *Phys. Rev.* **D99** (2019) 123014, [[1903.00022](#)].
- [17] S. Shalgar and I. Tamborra, *On the Occurrence of Crossings Between the Angular Distributions of Electron Neutrinos and Antineutrinos in the Supernova Core*, *Astrophys. J.* **883** (2019) 80, [[1904.07236](#)].
- [18] M. Delfan Azari, S. Yamada, T. Morinaga, W. Iwakami, H. Okawa, H. Nagakura et al., *Linear Analysis of Fast-Pairwise Collective Neutrino Oscillations in Core-Collapse Supernovae based on the Results of Boltzmann Simulations*, *Phys. Rev.* **D99** (2019) 103011, [[1902.07467](#)].
- [19] A. Merle, *Sterile Neutrino Dark Matter*. IOP, 2017, [10.1088/978-1-6817-4481-0](#).
- [20] A. Boyarsky, M. Drewes, T. Lasserre, S. Mertens and O. Ruchayskiy, *Sterile Neutrino Dark Matter*, *Prog. Part. Nucl. Phys.* **104** (2019) 1–45, [[1807.07938](#)].
- [21] K. N. Abazajian et al., *Light Sterile Neutrinos: A White Paper*, [1204.5379](#).
- [22] K. N. Abazajian and A. Kusenko, *Hidden Treasures: sterile neutrinos as dark matter with miraculous abundance, structure formation for different production mechanisms, and a solution to the sigma-8 problem*, [1907.11696](#).
- [23] Z. Xiong, M.-R. Wu and Y.-Z. Qian, *Active-sterile Neutrino Oscillations in Neutrino-driven Winds: Implications for Nucleosynthesis*, [1904.09371](#).
- [24] E. Pillumbi, I. Tamborra, S. Wanajo, H.-T. Janka and L. Hüdepohl, *Impact of neutrino flavor oscillations on the neutrino-driven wind nucleosynthesis of an electron-capture supernova*, *Astrophys. J.* **808** (2015) 188, [[1406.2596](#)].
- [25] I. Tamborra, G. G. Raffelt, L. Hüdepohl and H.-T. Janka, *Impact of eV-mass sterile neutrinos on neutrino-driven supernova outflows*, *JCAP* **1201** (2012) 013, [[1110.2104](#)].

- [26] M.-R. Wu, T. Fischer, L. Huther, G. Martínez-Pinedo and Y.-Z. Qian, *Impact of active-sterile neutrino mixing on supernova explosion and nucleosynthesis*, *Phys. Rev.* **D89** (2014) 061303, [[1305.2382](#)].
- [27] H. Nunokawa, J. T. Peltoniemi, A. Rossi and J. W. F. Valle, *Supernova bounds on resonant active sterile neutrino conversions*, *Phys. Rev.* **D56** (1997) 1704–1713, [[hep-ph/9702372](#)].
- [28] K. C. Y. Ng, B. M. Roach, K. Perez, J. F. Beacom, S. Horiuchi, R. Krivonos et al., *New Constraints on Sterile Neutrino Dark Matter from NuSTAR M31 Observations*, *Phys. Rev.* **D99** (2019) 083005, [[1901.01262](#)].
- [29] X. Shi and G. Sigl, *A Type II supernovae constraint on electron-neutrino - sterile-neutrino mixing*, *Phys. Lett.* **B323** (1994) 360–366, [[hep-ph/9312247](#)].
- [30] J. Hidaka and G. M. Fuller, *Sterile Neutrino-Enhanced Supernova Explosions*, *Phys. Rev.* **D76** (2007) 083516, [[0706.3886](#)].
- [31] J. Hidaka and G. M. Fuller, *Dark matter sterile neutrinos in stellar collapse: Alteration of energy/lepton number transport and a mechanism for supernova explosion enhancement*, *Phys. Rev.* **D74** (2006) 125015, [[astro-ph/0609425](#)].
- [32] C. A. Argüelles, V. Brdar and J. Kopp, *Production of keV Sterile Neutrinos in Supernovae: New Constraints and Gamma Ray Observables*, *Phys. Rev.* **D99** (2019) 043012, [[1605.00654](#)].
- [33] M. Warren, G. J. Mathews, M. Meixner, J. Hidaka and T. Kajino, *Impact of sterile neutrino dark matter on core-collapse supernovae*, *Int. J. Mod. Phys.* **A31** (2016) 1650137, [[1603.05503](#)].
- [34] G. G. Raffelt and S. Zhou, *Supernova bound on keV-mass sterile neutrinos reexamined*, *Phys. Rev.* **D83** (2011) 093014, [[1102.5124](#)].
- [35] MPA Supernova Archive, <https://wwwmpa.mpa-garching.mpg.de/ccsnarchive>.
- [36] M. T. Keil, G. G. Raffelt and H.-T. Janka, *Monte Carlo study of supernova neutrino spectra formation*, *Astrophys. J.* **590** (2003) 971–991, [[astro-ph/0208035](#)].
- [37] I. Tamborra, B. Müller, L. Hüdepohl, H.-T. Janka and G. G. Raffelt, *High-resolution supernova neutrino spectra represented by a simple fit*, *Phys. Rev.* **D86** (2012) 125031, [[1211.3920](#)].
- [38] S. P. Mikheev and A. Yu. Smirnov, *Neutrino Oscillations in a Variable Density Medium and Neutrino Bursts Due to the Gravitational Collapse of Stars*, *Sov. Phys. JETP* **64** (1986) 4–7, [[0706.0454](#)].
- [39] S. P. Mikheyev and A. Yu. Smirnov, *Resonance enhancement of oscillations in matter and solar neutrino spectroscopy*, *Yadernaya Fizika* **42** (1985) 1441–1448.
- [40] L. Wolfenstein, *Neutrino oscillations in matter*, *Phys. Rev. D* **17** (May, 1978) 2369–2374.
- [41] C. W. Kim, W. K. Sze and S. Nussinov, *On Neutrino Oscillations and the Landau-zener Formula*, *Phys. Rev.* **D35** (1987) 4014.
- [42] S. J. Parke, *Nonadiabatic Level Crossing in Resonant Neutrino Oscillations*, *Phys. Rev. Lett.* **57** (1986) 1275–1278.
- [43] G. G. Raffelt and G. Sigl, *Neutrino flavor conversion in a supernova core*, *Astropart. Phys.* **1** (1993) 165–184, [[astro-ph/9209005](#)].
- [44] K. Abazajian, G. M. Fuller and M. Patel, *Sterile neutrino hot, warm, and cold dark matter*, *Phys. Rev.* **D64** (2001) 023501, [[astro-ph/0101524](#)].
- [45] R. Bollig, H.-T. Janka, A. Lohs, G. Martínez-Pinedo, C. J. Horowitz and T. Melson, *Muon Creation in Supernova Matter Facilitates Neutrino-driven Explosions*, *Phys. Rev. Lett.* **119** (2017) 242702, [[1706.04630](#)].

- [46] T. Leitner, L. Alvarez-Ruso and U. Mosel, *Neutral current neutrino-nucleus interactions at intermediate energies*, *Phys. Rev.* **C74** (2006) 065502, [[nucl-th/0606058](#)].
- [47] S. Hannestad and G. G. Raffelt, *Supernova neutrino opacity from nucleon-nucleon Bremsstrahlung and related processes*, *Astrophys. J.* **507** (1998) 339–352, [[astro-ph/9711132](#)].
- [48] G. G. Raffelt, *Stars as laboratories for fundamental physics*. Chicago, USA: Univ. Pr. (1996) 664 p, 1996.
- [49] D. Q. Lamb and C. J. Pethick, *Effects of neutrino degeneracy in supernova models*, *Astrophys. J.* **209** (1976) L77–L81.
- [50] S. W. Bruenn, *Stellar core collapse: Numerical model and infall epoch*, *Astrophys. J. Suppl.* **58** (1985) 771–841.